On the Workspace of Electromagnetic Navigation Systems

Journal Article

Author(s):
Boehler, Quentin (iD); Gervasoni, Simone; Charreyron, Samuel (iD); Chautems, Christophe; Nelson, Bradley (iD)

On the Workspace of Electromagnetic Navigation Systems

Quentin Boehler, *Member, IEEE,* Simone Gervasoni, Samuel L. Charreyron, Christophe Chautems, and Bradley J. Nelson, *Fellow, IEEE*

Abstract—In remote magnetic navigation, a magnetic navigation system is used to generate magnetic fields to apply mechanical wrenches to steer a magnetic object. This technique can be applied to navigate untethered micro- and nanorobots, as well as tethered magnetic surgical tools for minimally invasive medicine. The design and characterization of these systems have been extensively investigated over the past decade. The determination of the region in space in which these systems can operate has yet to be formalized within the research community. This region is commonly referred to as the "workspace" and constitutes a central concept for any class of robotic system. We focus on magnetic navigation systems comprised of electromagnets and propose a first set of definitions for a magnetic workspace, a methodology to determine it, and evaluation metrics to analyse its characteristics. Our methodology and tools are illustrated with several examples of planar and spatial electromagnetic magnetic navigation systems for both didactic and realistic navigation scenarios.

Index Terms—Electromagnetic navigation system, workspace, remote magnetic navigation.

I. INTRODUCTION

REMOTE magnetic navigation (RMN) is an actuation technology in which magnetic fields are used to navigate devices containing magnetic material [1]. This technology is particularly promising for minimally invasive surgery, as it allows soft and bio-compatible micro- and nanorobots to be navigated remotely [2], [3]. The manipulation of magnetic catheters in particular receives considerable research attention primarily due to the potential for increased safety, reduced invasiveness, and high dexterity in a broad variety of surgical procedures [4]–[7]. New technologies for medical applications of RMN are also being actively investigated, such as variable stiffness features [8], *in situ* bio-printing of magnetic catheters [9], and the development of advanced actuation strategies [10]. Several companies have proposed the use of RMN for the magnetic navigation of cardiac catheters in clinics, including Stereotaxis Inc. [11] and Aeon Scientific AG[1], with more than 140,000 procedures completed so far with this modality [12].

In RMN, the magnetic fields are generated by a magnetic navigation system (MNS). Electromagnetic navigation systems (eMNS) are a class of MNS that are composed of electromagnets, where the magnetic fields are modulated by the amount of electrical current running through conductive

The authors are with the Multi-Scale Robotics Lab, ETH Zurich, Switzerland.

[1]Aeon Scientific AG is a former spin-off company of the Multi-Scale Robotics Lab.
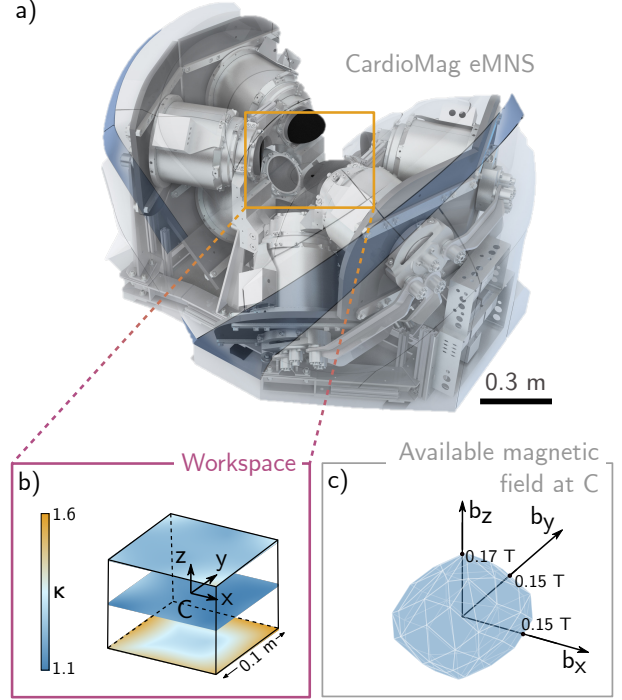

Fig. 1. Workspace and magnetic tasks of an Electromagnetic Navigation System. a) The CardioMag eMNS, an eight-coil pre-clinical prototype. b) Magnetic-Feasible Workspace (colored area) evaluated at three different heights of a cubic volume of side $0.1\,\text{m}$, and condition number κ (see definition of κ in section V-C, and detailed study in section VI-C1). c) Available magnetic field generated at the center C of the volume. The blue polyhedron represents the available field components b_x, b_y and b_z along the axes x, y and z.

windings. The CardioMag, a pre-clinical prototype of eMNS developed by Aeon Scientific AG, is depicted in Fig. 1a. It is composed of eight coils that are arranged so that a porcine model can fit on a patient bed between its coils. An example of an eMNS composed of two electromagnets of currents i_1 and i_2 is depicted in Fig. 2a, and shows the magnetic field lines generated by the electromagnets within their mid-plane. The magnetic field interacts with the magnetic object to be manipulated, producing magnetic forces and torques for its navigation. As such, an eMNS is a type of robotic manipulator that produces a given magnetic field at a position in space by controlling the currents in its electromagnets. For clinical systems, the electromagnets can be arranged near or around the body of a patient to produce magnetic fields suitable for a given navigation task.

While the modeling and design of eMNSs have been exten-

sively discussed over the past decade [13]–[16], their evaluation in a standardized manner has not been fully considered. In [17], Pourkand et al. discuss different eight-coil system designs and provide a critical analysis of the performance of the system at a single position in space. However, there seems to be no consensus or unified opinion on the evaluation tools and metrics for an eMNS. The concept of *workspace* has also not yet been clearly defined for an eMNS. This concept is closely related to one's ability to evaluate the capability of the eMNS to perform its task at any position in space. The design of eMNSs has been an active research area for over 15 years, with many recent works putting considerations related to the systems' workspace and magnetic performances at the center of their research. Several works thus investigated different metrics and methods to study and design their own eMNS for specific applications [18]–[24]. However, despite the large variety of contributions of these works, it appears to us that none have been trying to propose generic and standardized definitions and metrics so far, which would benefit this research community as a whole.

This paper proposes definitions for the workspace of an eMNS together with the tools to evaluate its performance under practical constraints, such as limitations on electromagnet currents. These tools are designed to be easily re-used by any designer and user of an eMNS to evaluate and control their system and to describe its performance in a standardized manner. Evaluation of the workspace is challenging as it is related to the targeted application, namely manipulating a magnetic object. We address this challenge by offering tools that can be used for any robotic task, which is defined either in terms of the magnetic fields or the mechanical wrenches that the fields induce on a magnetic object. We believe that this paper provides a seminal framework to standardize the analysis of an eMNS and comprehensive examples of its application to realistic systems and tasks.

The companion code to reproduce our results is available on CodeOcean [2]. In appendix A, we provide a description of the elements in the code relevant to understand, implement and reproduce the methods and results of the paper.

In section II, we introduce the terminology adopted in the paper. In section III, we propose several definitions [3] for the workspace of an eMNS. Section IV provides a methodology to estimate the workspace, and section V proposes evaluation metrics to analyse the performance of eMNSs for given tasks. In section VI, we apply this methodology to numerous 2d and 3d examples, including the CardioMag eMNS, a pre-clinical eight-coil prototype. We also provide experimental verification of this approach on a new three-coil system called Navion in section VII. Sections VIII and IX provide an extensive discussion of our contributions and results and conclude our work.

---

[2]https://doi.org/10.24433/CO.2090933.v1

[3]A summary of the acronyms and definitions introduced in this paper is provided in appendix B.

II. TERMINOLOGY

A. Remote magnetic navigation

At each position $\mathbf{p} \in \mathbb{R}^3$, an eMNS provides a mapping g between the electrical currents $\mathbf{i} \in \mathbb{R}^n$ running through the n electromagnets (which we will refer to as *coils* in the rest of the paper) and the magnetic field $\mathbf{b} \in \mathbb{R}^3$.

$$\mathbf{b}(\mathbf{p}) = g(\mathbf{p}, \mathbf{i}). \tag{1}$$

Forces and torques are generated on magnetic objects, which interact with the magnetic field. In many cases, it is sufficient to represent discrete magnets by single dipoles centered on their center of mass and with the dipole moment $\mathbf{m}$ pointing in the direction of their average magnetization. This covers several manipulation cases, including the manipulation of untethered magnetic microrobots and magnetic catheters composed of a permanent distal magnet at their tip. The magnetic torques $\mathbf{t}$ and forces $\mathbf{f}$ applied on the magnetic dipole are expressed as [1]

$$\mathbf{t} = \mathbf{m} \times \mathbf{b} \tag{2}$$
$$\mathbf{f} = (\mathbf{m} \cdot \nabla)\mathbf{b} \tag{3}$$

where the field gradient $\nabla\mathbf{b}$ is a 3×3 tensor. As the field is both curl-free and divergence-free in free space, we usually prefer to express the five independent components of the tensor as the vector $\mathbf{g} = \begin{bmatrix} \frac{\partial b_x}{\partial x} & \frac{\partial b_x}{\partial y} & \frac{\partial b_x}{\partial z} & \frac{\partial b_y}{\partial y} & \frac{\partial b_y}{\partial z} \end{bmatrix}^T$ with $\mathbf{b} = \begin{bmatrix} b_x & b_y & b_z \end{bmatrix}^T$ when expressed in a reference base frame. The previous equations can therefore be conveniently expressed in the following forms

$$\mathbf{t} = \mathbf{T}(m, \alpha, \beta)\mathbf{b} \tag{4}$$
$$\mathbf{f} = \mathbf{F}(m, \alpha, \beta)\mathbf{g} \tag{5}$$

where α and β are angles that represent the orientation of $\mathbf{m}$ in the reference frame and $m = ||\mathbf{m}||$. The expressions of $\mathbf{T}(m, \alpha, \beta)$ and $\mathbf{F}(m, \alpha, \beta)$ are provided in appendix C.

A linear relationship is usually assumed between the currents and the field and its gradient via an *actuation matrix* $\mathbf{A} \in \mathbb{R}^{8 \times n}$ so that [1]

$$\begin{bmatrix} \mathbf{b} \\ \mathbf{g} \end{bmatrix} = \begin{bmatrix} \mathbf{A}_b \\ \mathbf{A}_g \end{bmatrix} \mathbf{i} = \mathbf{A}\,\mathbf{i}. \tag{6}$$

We refer to $\mathbf{A}_b$ and $\mathbf{A}_g$ as the *field* and *gradient actuation matrix*, respectively.

B. Robotic task

Classic robotic manipulators such as serial robot arms are composed of motorized joints, where torques are controlled to generate a mechanical wrench with its end-effector. A manipulator linearly maps the joint torques (inputs) to the mechanical wrench (output) via a Jacobian matrix. The output of the system can be referred to as a *task space*, in the sense that the role of the robot is to perform a task with its end-effector, e.g. to generate a mechanical wrench.

In a similar manner, the inputs of an eMNS are the currents flowing through the windings of the coils, which are limited by several practical factors including power consumption and the maximum current capacity of the coils. The choice of its output, or task, is made ambiguous by the fact that the manipulation of a magnetic object ultimately comes from the interaction between this object and the magnetic field generated by the eMNS. It is thus relevant to specifically consider two types of tasks:

- A *magnetic task* defined in terms of the magnetic field and the gradient to be generated by the eMNS. It is independent from the magnetic object to be manipulated.
- A *wrench task* defined in terms of magnetic torques and forces to be applied on the magnetic object.

A *magnetic task* is related to the intrinsic properties of the eMNS regardless of the nature of the object to be manipulated. The *wrench task* is required to manipulate a specific magnetic device, and is intrinsically dependent on a corresponding *magnetic task*.

In order to provide consistent terminology for the paper, we refer to the vector describing a task as a *task vector* and denote it $\boldsymbol{\tau}$. The task vector can be composed of any component or combination of components of $\begin{bmatrix} \mathbf{b} & \mathbf{g} \end{bmatrix}^T$ (resp. $\begin{bmatrix} \mathbf{t} & \mathbf{f} \end{bmatrix}^T$) for a magnetic task (resp. wrench task). We define the *task actuation matrix* $\mathbf{A}_\tau$, which relates to the current vector to the task vector as

$$\boldsymbol{\tau} = \mathbf{A}_\tau \mathbf{i}. \tag{7}$$

The matrix $\mathbf{A}_\tau$ is composed of the lines, or the line combinations of $\mathbf{A}$ for the corresponding components of the task vector (e.g. if $\boldsymbol{\tau} = \mathbf{b}$, then $\mathbf{A}_\tau = \mathbf{A}_b$). Unlike the case of a wrench task, this matrix is independent of the orientation of the magnetic object for the magnetic task. More generally, we consider any task that is independent of the magnetic object to be navigated as a magnetic task.

The mapping between the input currents of an eMNS and a magnetic task through $\mathbf{A}_\tau$ is illustrated in Fig. 2b for a system composed of two coils, and a two-dimensional magnetic task defined here by the components of the magnetic field b_x and b_y in the plane $x - y$. Feeding the coils of the eMNS with currents i_1 and i_2 generates a magnetic field. The field lines are depicted in Fig. 2a in the plane $x - y$ as an example.

C. Workspace and feasibility

The *reachable workspace* of a classic robotic manipulator is usually defined as the set of positions in space that can be reached by its end-effector [25]. This workspace is bound by configurations where the robot is said to be *singular* [26]. However, this definition is not wholly applicable in the case of an eMNS that interacts with the magnetic object and creates the magnetic field remotely through non-moving coils. Due to the lack of a proper kinematic chain, an eMNS does not exhibit singular configurations as limit configurations, and the concept of a reachable workspace is not appropriate for the workspace of an eMNS.
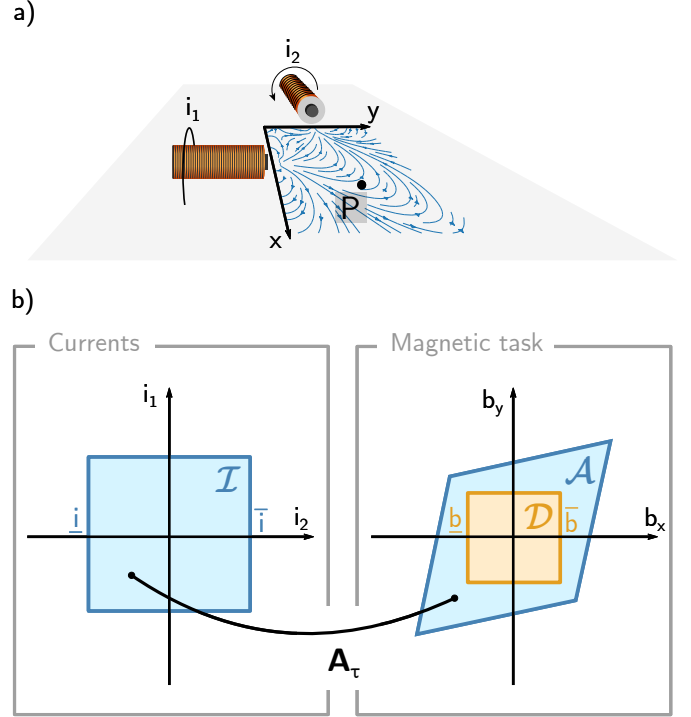

Fig. 2. A two-coil planar eMNS. a) Illustration of the system. b) Feasible task at the position P (same as in Fig. 4a with $\theta = 90°$). The task consists of the components of the magnetic field b_x and b_y in the plane $x - y$.

A more promising approach is to use the concept of a *wrench feasible workspace* that was originally developed for cable-driven parallel robots (CDPRs) [27]. CDPRs are composed of a platform whose position is controlled by a set of cables in tension. Due to this particular mode of parallel actuation, the platform must be able to counteract a set of external wrenches, such as the weight of the platform, while keeping its cables in tension. The concept of *wrench feasibility* stems from the idea that for a given pose, the platform must be able to achieve a desired set of tasks around the specific constraints of its actuators [28]. These tasks are application specific, and the constraints on the actuators usually stem from practical considerations (e.g. the tension in the cables of a CDPR must be positive and below a maximum value).

In a similar manner, an eMNS must be able to achieve a user-defined desired set of tasks $\mathcal{D}$, while the currents in its coils must remain within a user-defined set of admissible currents $\mathcal{I}$. At any position $\mathbf{p}$, one can determine an available set of tasks $\mathcal{A}$ composed of the tasks that the eMNS can perform under the constraints $\mathbf{i} \in \mathcal{I}$. At a position $\mathbf{p}$, the set of tasks $\mathcal{D}$ is then said to be *feasible* if the following condition is met:

$$\mathcal{D} \subseteq \mathcal{A} \tag{8}$$

meaning that all of the desired tasks can be achieved for admissible currents at this position. The feasibility is illustrated in Fig. 2b for the previously introduced two-coil system and a two-dimensional magnetic task. This illustrates how the set

of admissible currents $\mathcal{I}$ maps to the available set of tasks $\mathcal{A}$. In this example, the desired set of tasks $\mathcal{D}$ represented on the right side of Fig. 2b is feasible, as it respects inclusion (8).

III. DEFINITIONS

A. Workspace of an eMNS

Our objective is to provide a useful set of tools to compare and analyze the workspace of an eMNS in a standardized manner. Although some previous work [15], [29] introduced specific definitions based on application-specific considerations, there is no generic propositions on these.

We propose to define the workspace of an eMNS as the *set of positions in space where a desired set of tasks are feasible, given a set of admissible currents*. In the case of a given *magnetic* and *wrench task* as previously introduced, we also provide the following specific definitions that may be of interest for the standard analysis of an eMNS.

a) Definition 1: The *magnetic-feasible workspace* (MFW) of an eMNS is defined as the set of positions where a desired set of magnetic tasks is feasible, given a set of admissible currents.

b) Definition 2: The *wrench-feasible workspace* (WFW) of an eMNS is defined as the set of positions in space where a desired set of wrench tasks is feasible, given a set of admissible currents.

B. Admissible currents and desired tasks

The determination of the workspace therefore requires the user to specify the set $\mathcal{I}$ of admissible currents and a desired set of tasks $\mathcal{D}$.

The set $\mathcal{I}$ can take different forms depending on the requirements of the system. Two forms encompass most of the uses required of an eMNS. If working under strict power requirements, $\mathcal{I}$ is preferably formulated to limit the weighted sum of the square of the currents [4]. This formulation may, however, be too conservative when the system is not limited by its maximum power, but rather by the individual maximum currents in the coils, as can be the case for smaller systems. In this case, the infinity-norm of $\mathbf{i}$, i.e. the maximum current admissible in the coil, must be limited. This case defines $\mathcal{I}$ as

$$\mathcal{I} = \{\mathbf{i} \in \mathbb{R}^n \mid \underline{\mathbf{i}} \leq \mathbf{i} \leq \bar{\mathbf{i}}\} \tag{9}$$

where $\underline{\mathbf{i}}$ (resp. $\bar{\mathbf{i}}$) is the vector which components are the minimum (resp. maximum) admissible currents in each coil. An example of this type of set is illustrated in the case of the two-coil eMNS in Fig. 2b with $\underline{\mathbf{i}} = \begin{bmatrix} \underline{i} & \underline{i} \end{bmatrix}^T$ and $\bar{\mathbf{i}} = \begin{bmatrix} \bar{i} & \bar{i} \end{bmatrix}^T$.

The choice of the components of the task vector and $\mathcal{D}$ depends on the intended use of the eMNS for a given application. Set $\mathcal{D}$ is composed of the task vectors $\boldsymbol{\tau}$ that the system must achieve. For example, a typical desired set of magnetic tasks for a three-coil eMNS is

$$\mathcal{D} = \{\mathbf{b} \in \mathbb{R}^3 \mid ||\mathbf{b}||_2 \leq \bar{b}\} \tag{10}$$

where $\boldsymbol{\tau} = \mathbf{b}$. This specifies that the system must be able to generate a magnetic field $\mathbf{b}$ of a maximum magnitude $\bar{b}$ in any direction in space. This approach is relevant when one wants to steer a magnetic catheter with the eMNS and formulates a requirement on the minimum magnetic field magnitude that the system must achieve to steer it. With this formulation, the magnetic field gradient is not taken into account. This is relevant for catheter steering in which the magnetic forces induced by the gradient usually have little affect on the tool compared to the torques induced by the magnetic field. Conversely, for a task composed only of the gradient, a gradient within the available set of tasks do not account for any requirements on the magnetic field direction and magnitude.

An eMNS cannot perform a wrench task of a dimension higher than five, because a torque cannot be applied along the main axis of the magnetic body being manipulated. In [30], it is shown that a minimum of eight coils is necessary to achieve five degree-of-freedom (DOF) motion. For a magnetic task, the dimension d of the task vector must satisfy $d \leq n$.

IV. WORKSPACE ESTIMATION

In the following, we provide a methodology to estimate the MFW and the WFW. This includes the determination of $\mathcal{A}$ for any desired set of magnetic tasks, and methods to evaluate the feasibility of these tasks at any position in space.

We assume that the eMNS behaves in a linear manner, and that one can estimate the actuation matrix $\mathbf{A}_\tau$ at any position in space after having calibrated the system using a linear model, such as the one proposed in [13].

We only consider admissible current sets of the form (9), which we find to be the most relevant type of set to evaluate an eMNS, in general.

A. Feasibility of magnetic tasks

1) Available set of tasks: To evaluate the feasibility of a magnetic task we must first estimate $\mathcal{A}$ given $\mathcal{I}$. We make use of a *hyperplane shifting* method to do this, as previously applied for CDPRs [28]. This involves determining a hyperplane representation of $\mathcal{A}$ given that the currents are constrained as in (9). With this approach, the set $\mathcal{A}$ is represented by a zonotope, a special class of convex polytopes which number of vertices depends on the number of coils of the eMNS [5].

Our method consists of the following steps [6]:

1) Build a matrix $\mathbf{M}$ formed by $d-1$ linearly independent columns extracted from the $(d \times n)$ matrix $\mathbf{A}_\tau$, and build a vector $\mathbf{v}$ orthogonal to these columns. The linear dependency of the extracted columns of $\mathbf{A}_\tau$ can be checked by computing the rank of $\mathbf{M}$, and $\mathbf{v}$ can be

---

[4]This defines $\mathcal{I}$ as the set of current vectors $\{\mathbf{i} \in \mathbb{R}^n \mid \mathbf{i}^T \mathbf{Z} \mathbf{i} \leq \overline{P}\}$ where $\mathbf{Z}$ is a diagonal matrix with the coil resistances on its diagonal, and $\overline{P}$ is the limiting power.

[5]More information on the mathematical tools this section relies on can be found in [28] and in the companion code of our paper.

[6]In our companion code, this algorithm is implemented in the function HyperPlaneShiftingMethod in utilities.ipynb.

obtained as the cross product of all of the column vectors in $\mathbf{M}$ when $d \leq 3$. For higher dimensions, this vector can be obtained by picking any vector in the base of the nullspace of $\mathbf{MM}^T$.

2) Build the vector $\mathbf{n}$ as

$$\mathbf{n} = \mathbf{v}/\|\mathbf{v}\| \tag{11}$$

which is the unit vector perpendicular to the initial hyperplane that includes these $d - 1$ columns.

3) Build the vector $\mathbf{l}$ as

$$\mathbf{l} = \mathbf{W}^T\mathbf{n} \tag{12}$$

where $\mathbf{W}$ is a matrix whose columns are the remaining $n - d + 1$ column vectors of $\mathbf{A}_\tau$, so that the components l_i of $\mathbf{l}$ are the projection of these vectors on $\mathbf{n}$.

4) Build the support hyperplanes $\mathbf{p}_+$ and $\mathbf{p}_-$ along $\mathbf{n}$ and $-\mathbf{n}$ as

$$\mathbf{p}_+ = h_+\mathbf{A}_\tau\underline{\mathbf{i}} \tag{13}$$
$$\mathbf{p}_- = h_-\mathbf{A}_\tau\underline{\mathbf{i}} \tag{14}$$

with

$$h_+ = \max\left(\sum_{j=1}^{n-d+1} \alpha_j \Delta i_j l_j, \alpha_j \in \{0,1\}\right) \tag{15}$$
$$h_- = \min\left(\sum_{j=1}^{n-d+1} \alpha_j \Delta i_j l_j, \alpha_j \in \{0,1\}\right) \tag{16}$$
$$\tag{17}$$

and Δi_j the components of $\Delta\mathbf{i}$ defined as $\bar{\mathbf{i}} - \underline{\mathbf{i}}$. Note that a combination matrix can be used to evaluate h_+ and h_-.

5) Compute the matrix $\mathbf{N}_i$ and the vector $\mathbf{d}_i$ as

$$\mathbf{N}_i = \begin{bmatrix} \mathbf{n} & -\mathbf{n} \end{bmatrix}^T \tag{18}$$
$$\mathbf{d}_i = \begin{bmatrix} \mathbf{n}^T\mathbf{p}_+ & -\mathbf{n}^T\mathbf{p}_- \end{bmatrix}^T \tag{19}$$

which constitute the hyperplane representation of the current combination.

6) Repeat step 2 to 5 for all $d - 1$ combinations in $\mathbf{A}_\tau$. Note that a permutation matrix can be used to exhaust all of the $d - 1$ combinations of vectors in $\mathbf{A}_\tau$.

7) Build the matrix $\mathbf{N}$ and the vector $\mathbf{d}$ as the vertical stacking of $\mathbf{N}_i$ and $\mathbf{d}_i$ obtained for all $i \in [\![1 \ ; \ d-1]\!]$.

With this hyperplane representation $(\mathbf{N}, \mathbf{d})$, the available set $\mathcal{A}$ is expressed as the following set of task vectors

$$\mathcal{A} = \{\boldsymbol{\tau} \in \mathbb{R}^d \mid \mathbf{N}\boldsymbol{\tau} \leq \mathbf{d}\}. \tag{20}$$

The hyperplanes are illustrated in a simple example in Fig. 3. The vector $\mathbf{p}_+$ corresponding to the first hyperplane is represented, as well as the scalar d_1 (first component of

vector $\mathbf{d}_i$) obtained from its projection on the hyperplane's normal $\mathbf{n}_1$. By comparing Fig. 2b and Fig. 3, it can be noted that the number of hyperplanes which constitute the sides of $\mathcal{A}$, depends on the number of coils of the eMNS (parallelogram for the two-coil system, and octagon for the four-coil system).
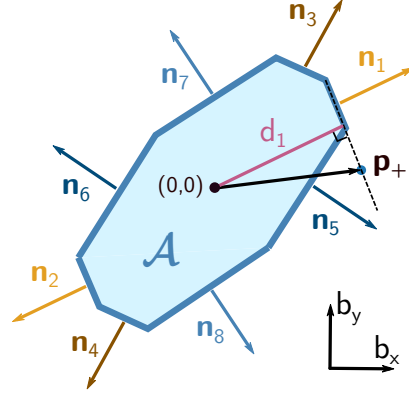

Fig. 3. Illustration of the normal vectors of the hyperplanes in the case of a four-coil eMNS (position B for the system depicted in Fig. 5b). The task consists of the components b_x and b_y of the field in the plane. The hyperplanes are normal to four pairs of opposite unit vectors.

2) Evaluation of the feasibility: Once the hyperplane representation of $\mathcal{A}$ is known, the evaluation of the feasibility consists in verifying the inclusion (8). This evaluation depends on the nature of $\mathcal{D}$. We introduce the three most common cases in the following. These cases are thoroughly described in [28] to compute available wrench sets for CDPRs. The interested reader is encouraged to refer to this work for more details, as we only provide limited explanations on these within the scope of this paper. Detailed and commented implementations of these functions are also available in our companion code (see Appendix A).

a) Discrete set: if $\mathcal{D}$ is composed of a discrete set of task vectors $\{\boldsymbol{\tau}_1 \ldots \boldsymbol{\tau}_N\}$, the feasibility can be trivially derived from the definition of $\mathcal{A}$ in (20) and is verified if the following inequality stands for all $i \in [\![1 \ ; \ N]\!]$

$$\mathbf{N}\boldsymbol{\tau}_i \leq \mathbf{d} \tag{21}$$

meaning that each $\boldsymbol{\tau}_i$ is a subset of $\mathcal{A}$.

b) Polytope: if $\mathcal{D}$ is a convex polytope, the feasibility is verified if the following inequality stands

$$\mathbf{NV} \leq \mathbf{d} \tag{22}$$

where $\mathbf{V}$ is a matrix whose columns are the vertices of the polytope. An example of a feasible set of tasks $\mathcal{D}$ is illustrated in the case of a two-coil eMNS in Fig. 2.

c) Ellipsoid: if $\mathcal{D}$ is an ellipsoid of half-axes $(e_1 \ldots e_d)$, the feasibility is verified if all of the following task vectors $\boldsymbol{\tau}_i$ are feasible

$$\boldsymbol{\tau}_i = \pm\frac{\text{diag}(e_1^2 \ldots e_d^2)\mathbf{n}_i^T}{\sqrt{(e_1 n_{i1})^2 + \cdots + (e_d n_{id})^2}} \tag{23}$$

where $\mathbf{n}_i = \begin{bmatrix} n_{i1} \ldots n_{id} \end{bmatrix}$ is the i-th line of $\mathbf{N}$.

B. Feasibility of wrench tasks

Determining the feasibility of wrench tasks is much more complex. This is due to the fact that feasibility must be verified for any orientation of the magnetic object to be manipulated, which leads to a high dimensional problem that is difficult to address [15].

Here, we propose what we believe is a relevant approach to later provide a conservative estimate of the WFW. The overall idea is to formulate a specific desired set of magnetic tasks $\mathcal{D}$, whose feasibility constitutes a sufficient condition to the feasibility of the desired wrench task. In the following, we approach the problem independently for a 2-dimensional task in torques and a 3-dimensional task in forces, which constitute, in our opinion, to the two most interesting for broad use in remote magnetic navigation.

1) Torque: As previously explained in (2), a magnetic torque $\mathbf{t}$ is linearly mapped to the magnetic field $\mathbf{b}$ via a skew-symmetric matrix $\mathbf{T}$. In order to ensure that a torque task can be performed for any orientation of the magnetic dipole, one can see that $\mathbf{T}$ maps a unitary sphere into a circle of radius m. The normal vector of the circle is along the axis of the dipole moment. This can be easily verified through the singular value decomposition of $\mathbf{T}$ for any orientation described by the pair (α, β), and noticing that the singular values are $\begin{pmatrix} m & m & 0 \end{pmatrix}$ along the two orthogonal axes and the longitudinal axis of the magnetic dipole, respectively. This is consistent with the fact that one cannot apply a torque along the magnetic dipole axis.

As a result, the feasibility of a magnetic task specified as the set of magnetic fields $\mathbf{b}$ within a sphere of radius $\bar{b}$ is sufficient to ensure that any torque along an axis orthogonal to $\mathbf{m}$ can be generated up to a magnitude $m\bar{b}$.

2) Force: In a similar fashion, we saw in (3) that a magnetic force $\mathbf{f}$ is linearly mapped to the magnetic field gradient $\mathbf{g}$ via a matrix $\mathbf{F}$. We can observe that $\mathbf{F}$ maps a unitary 5-dimensional sphere into a 3-dimensional ellipsoid. The lengths of the semi-axes of this ellipsoid can be determined via the singular values of $\mathbf{F}$, and are proportional to the force that can be applied on the magnetic dipole along the main axes of the ellipsoid in this configuration. The minimum singular value $\underline{\sigma}$ of $\mathbf{F}$ for $(\alpha, \beta) \in \mathbb{R}^2$ is thus proportional to the force magnitude that can be produced for any orientation of $\mathbf{m}$ and in any direction in space, assuming $\mathbf{g}$ is in a 5-dimensional sphere.

As a result, the feasibility of a magnetic task specified as the set of magnetic field gradients $\mathbf{g}$ within a 5-dimensional sphere of radius $\bar{g}$ is sufficient to ensure that any force can be generated at least up to a magnitude $\underline{\sigma}\bar{g}$ for any orientation of the magnetic dipole. For the matrix $\mathbf{F}$ introduced in the appendix, the value of $\underline{\sigma}$ can be found as $\approx 0.707m$.

C. Methodology for the determination of the workspace

The determination of a workspace consists of testing the feasibility of a desired set of tasks at positions within a given volume in space. Two main methods exist to do this. The most common and intuitive one is to discretize the space and test feasibility at each grid point. This method is straightforward to implement, but has the disadvantage that it does not guarantee feasibility between grid points, and may consequently overlook holes in the workspace.

Interval analysis is an alternative method that can address this disadvantage. This consists of testing the feasibility for full boxes in space. Together with a bisection strategy, this method can iteratively classify smaller and smaller boxes as inside or outside the workspace [31]. The main drawback of interval analysis is that it can be cumbersome to implement and requires a very fine bisection of the boxes if the interval evaluation is too conservative to successfully classify a box.

In this paper, we primarily propose to implement a discretization approach. In section VI-A3 however, we illustrate the use of an interval analysis, which is an interesting alternative for problems in low dimensions and when the feasibility within continuous regions of space must be guaranteed.

1) Magnetic Feasible Workspace: Once the components of the task vector are defined, the methodology given in Algorithm 1 can be followed to determine the MFW.

Algorithm 1 Determination of the MFW

$\mathcal{D} \leftarrow$ Desired magnetic tasks
$\bar{\mathbf{i}} \leftarrow$ Maximum admissible currents
$\underline{\mathbf{i}} \leftarrow$ Minimum admissible currents
$\mathcal{W}_t \leftarrow$ Positions to be tested
$\mathcal{W}_{in} \leftarrow \{\}$ //Positions in the MFW

for $\mathbf{p} \in \mathcal{W}_t$ **do**
    $\mathbf{A}_\tau \leftarrow$ ComputeTaskActuationMatrix($\mathbf{p}$)
    $\mathcal{A} \leftarrow$ HyperplaneShiftingMethod($\mathbf{A}_\tau, \bar{\mathbf{i}}, \underline{\mathbf{i}}$)
    IsPositionFeasible $\leftarrow$ VerifyFeasibility($\mathcal{A}, \mathcal{D}$)
    if IsPositionFeasible **then**
        $\mathcal{W}_{in} \leftarrow \mathcal{W}_{in} \cup \{\mathbf{p}\}$ //Add position to the workspace
    end if
end for

---

2) Wrench Feasible Workspace: We propose a method to provide a conservative estimate of the WFW in three types of wrench tasks. In all cases, the approach consists of defining a corresponding set of magnetic tasks whose feasibility sufficiently ensures the feasibility of the wrench tasks. The first two cases are as follows:

1) The task of generating a torque up to a maximum magnitude $\bar{t}$ along any direction perpendicular to $\mathbf{m}$: define $\mathcal{D}$ as the set of magnetic fields $\mathbf{b}$ within a sphere of radius $\bar{t}/m$.
2) The task of generating a force up to a maximum magnitude $\bar{f}$ along any direction in space: define $\mathcal{D}$ as the set of magnetic field gradients $\mathbf{g}$ within a sphere of radius $\bar{f}/\underline{\sigma}$.

The third case is a combination of the first two, namely the desired set of tasks corresponding to the five achievable DOFs of the wrench task. In this case, one can define $\mathcal{D}$ as the set of magnetic fields and magnetic gradient within an ellipsoid of semi-axes $\bar{t}/m$ along the field components, and $\bar{f}/\underline{\sigma}$ along the gradient components.

Once $\mathcal{D}$ has been defined as a set of magnetic tasks, determine the corresponding MFW (follow Algorithm 1). The

attained MFW is included in the WFW. This estimation is conservative as $\mathcal{D}$ overestimates the required magnetic field and/or magnetic field gradient in some directions and in some configurations to ensure that the desired wrench can be achieved for any orientation of $\mathbf{m}$. This is due to the fact that the feasibility of $\mathcal{D}$ is sufficient, but not necessary for the wrench task to be feasible.

V. EVALUATION METRICS

The workspace of a manipulator provides a measure of feasibility of the task. It does not, however, provide any indication of how well the task can be performed.

Several evaluation metrics have been proposed in the past to characterize robotic systems within their workspace. Most are based on the analysis of the singular values of their Jacobian matrix. However in the case of an eMNS it is not trivial to characterize it based on the singular values of an actuation matrix due to the mixture of units composing the task [15].

Approaches to either optimize or compare the performance of eMNS designs for specific tasks have been proposed, mainly based on this analysis [29], [32]. For instance, in [33], Thornley et al. proposed dimensionless performance indices based on the Buckingham Π theorem to compare different coil arrangements. In [34], Chen et al. also introduced several metrics to characterize eMNSs, which include definitions of the manipulability, as well as local and global indices. In the following, we summarized the most common metrics already introduced for the study of eMNSs, and propose a new criteria based on our current methodology.

A. Minimum field and gradient gains

In [30], Petruska et al. proposed comparing systems using the minimum singular values of $\mathbf{A}_b \mathcal{N}_{\mathbf{A}_g}$ (resp. $\mathbf{A}_g \mathcal{N}_{\mathbf{A}_b}$) with $\mathcal{N}_{\mathbf{X}}$, the normalized nullspace of a matrix $\mathbf{X}$. This is the smallest field (resp. gradient) gain that has the capability of independently specifying any gradient (resp. field). However, these are limited to systems composed of at least eight coils.

B. Manipulability

The *manipulability measure* is a metric introduced in [35] to quantify a manipulator's dexterity. A direct analogy of this principle for an eMNS considers the transformation of a hypersphere in the coil currents space through the task actuation matrix, as proposed in [32], [34]. The manipulability measure μ is then computed as

$$\mu = \sqrt{|\det(\hat{\mathbf{A}}_\tau \hat{\mathbf{A}}_\tau^T)|} \tag{24}$$

with $\hat{\mathbf{A}}_\tau = \mathbf{S}\mathbf{A}_\tau$. The matrix $\hat{\mathbf{A}}_\tau$ is a normalized version of $\mathbf{A}_\tau$ in order to account for the possible mixture of units within the components of the task vector (namely either [T] for magnetic field and [T/m] for magnetic field gradient). The scaling matrix $\mathbf{S}$ is diagonal, and its i-th diagonal element is the inverse of the maximum value that the i-th component of the task vector can take in $\mathcal{D}$. The metric μ is the product of the singular values of $\hat{\mathbf{A}}_\tau$, so that it is proportional to the volume

of the manipulability ellipsoid [35]. This index does not give information on the shape of the ellipsoid, but only on its volume. A high manipulability measure can, for example, be reached at position where some directions can be dramatically more amplified than others, leading to an important volume of the ellipsoid in spite of the poor isotropy of the behavior.

C. Condition number

To evaluate the isotropy of the system, we usually consider the condition number κ, which is an index to evaluate the shape of the manipulability ellipsoid. It consists of comparing the maximum and the minimum singular values of $\hat{\mathbf{A}}_\tau$ denoted $\overline{\sigma}_a$ and $\underline{\sigma}_a$, respectively [36]. It is computed as

$$\kappa = \frac{\overline{\sigma}_a}{\underline{\sigma}_a}. \tag{25}$$

As the singular values of $\hat{\mathbf{A}}_\tau$ are equal to the length of the manipulability ellipsoid's half-axes, a condition number of 1 means that the system amplifies its currents equally for any component of the task vector, in which case the system is said to be *isotropic* [36].

D. Global conditioning index

The *global conditioning index* (CGI) extends the idea of the condition number to the whole workspace to provide a global metric rather than a local one. It corresponds to the average value of $1/\kappa$ over a workspace W [36].

$$\text{CGI} = \frac{\int_W (1/\kappa)\,dW}{\int_W dW} \tag{26}$$

which can be approximated in a discretized case by

$$\text{CGI}_a = \frac{\sum_i^N (1/\kappa_i)}{N} \tag{27}$$

for N points regularly spaced in the investigated volume, and κ_i is the condition number at the i-th position. This index is between 0 and 1. The closer it comes to 1, the more isotropic the system is within the tested workspace.

E. Margin between the desired and available sets of tasks

The inclusion (8) provides feasibility criteria to evaluate whether a position belongs to the workspace or not. A way to provide a finer evaluation of a position is to consider how much this inclusion is valid. Analogous considerations have been investigated in the context of CDPRs, and led to the derivation of the *capacity margin index* (also called *minimum degree of constraint satisfaction*) which consists in estimating the margin between the desired wrench tasks and the capacity of the robot [37].

In the context of our analysis of the eMNSs' workspace, we introduce a metric that we will call the $\mathcal{D}$-$\mathcal{A}$ distance, which measures the minimal margin between the desired set $\mathcal{D}$, and the available set $\mathcal{A}$.
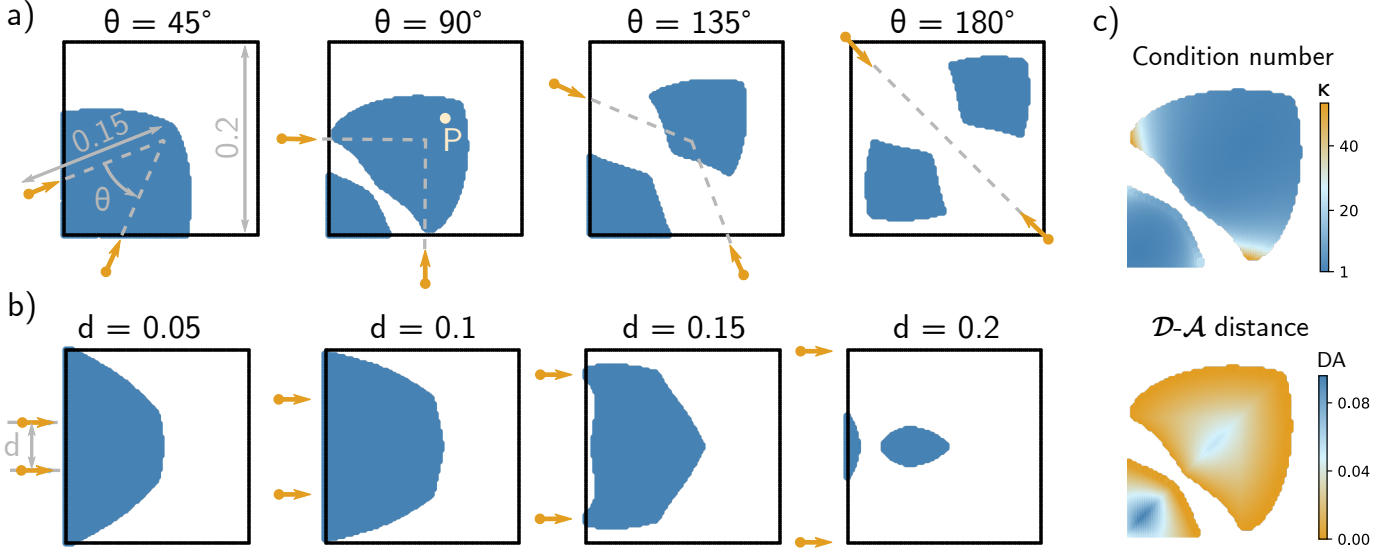
Fig. 4. MFW of an eMNS composed of two coils in a planar arrangement (for the sake of simplicity, these examples do not consider any physical units for the magnetic field magnitudes, the currents, and the distances). The positions within the MFW are represented in blue, and the dipole magnetic source of the coils are represented by the orange arrows. The tested area is represented by the black squares with sides of 0.2. The discretization grid within this area is 100×100. The admissible currents are $\bar{\mathbf{i}} = -\underline{\mathbf{i}} = \begin{bmatrix} 1.0 & 1.0 \end{bmatrix}^T$ and the maximum desired field is $\bar{b} = -\underline{b} = 0.02$. a) Influence of a variable opening angle between the sources direction. b) Influence of the distance between two parallel sources. c) Condition number and $\mathcal{D}$-$\mathcal{A}$ distance for the arrangement with $\theta = 90°$.

We derive the $\mathcal{D}$-$\mathcal{A}$ distance (denoted DA) from the generic definition (20) of $\mathcal{A}$ as follows:

$$\text{DA} = \min_{\boldsymbol{\tau} \in \mathcal{D}, j \in n_h} d_j - \mathbf{N}_j \boldsymbol{\tau} \tag{28}$$

with $\mathbf{N}_j$ the j-th line of $\mathbf{N}$, d_j the j-th component of $\mathbf{d}$, and n_h the number of hyperplanes used to represent $\mathcal{A}$. The term $\mathbf{N}_j \boldsymbol{\tau}$ represents the projection of a task $\boldsymbol{\tau}$ on the normal to the j-th hyperplane, while d_j represents the distance of this hyperplane to the origin (see Fig. 3). The $\mathcal{D}$-$\mathcal{A}$ distance corresponds to the smallest component of $\mathbf{d} - \mathbf{N}\boldsymbol{\tau}$ for $\boldsymbol{\tau} \in \mathcal{D}$, which is the minimal distance from any task in $\mathcal{D}$ to the hyperplanes of $\mathcal{A}$.

The evaluation of the metric depends on the type of desired tasks set $\mathcal{D}$ as presented in IV-A2. For a discrete set of tasks, each task in the set must be tested individually to find the minimum in (28). A similar case can be constructed for an ellipsoid using (23). For a polytope, the tasks to be tested are composed of the vertices of the polytope.

VI. APPLICATIONS

We illustrate the methodology through a series of examples both in 2d and 3d. The examples described in sections VI-A and VI-B are provided for an intuitive understanding of the shape of the workspace depending on the arrangement of the coils, and as a guide to use the evaluation metrics. For the sake of simplicity in these examples, each coil is modeled as a single dipole source, and all sources exhibit the same dipole coefficient. We did not consider any physical units to simplify our presentation. In section VI-C, we applied our methods to the CardioMag eMNS, an eight-coil system, using a magnetic model calibrated with experimental data, to show a more

realistic and practical case study following these simplified examples.

A. 2d systems

We first consider *2d systems*, where all of the coils lie in the same plane, and we analyse the performance of the system in this plane only. We consider a 2-dimensional magnetic task, composed of the components b_x and b_y of the magnetic field within the plane of the sources, and focus on the computation of the MFW for admissible currents in the form of (9), and a desired set of tasks of the following shape:

$$\mathcal{D} = \{(b_x, b_y) \in \mathbb{R}^2 \mid \underline{b} \leq (b_x, b_y) \leq \bar{b}\} \tag{29}$$

where the scalar values $\underline{b}$ and $\bar{b}$ represent the minimum and maximum desired field magnitude to be achieved respectively.

In the following examples, the tested area is a square with sides of 0.2. We use a discretization grid within this area of 100×100, and the maximum desired field is chosen as $\bar{b} = -\underline{b} = 0.02$. The admissible currents are $\bar{\mathbf{i}} = -\underline{\mathbf{i}} = \mathbf{1}$.

1) Two-coil systems: We investigate two situations that are of interest to understand the shape of the MFW for the arrangement of two coils in a plane and located at 0.15 from the center of the tested area: 1) the influence of the relative orientation of two coils at equal distance from the center of the tested area, 2) the influence of the distance between two parallel coils. The results for an eMNS composed of two coils in a planar arrangement are represented in Fig. 4.

In Fig. 4a, the MFW is illustrated for four different angles between the coils that are at equal distance from the center of the analysed area represented by the black square. The MFW gradually splits into two distinct regions. This can

be intuitively understood through the extreme case for 180°, where the generation of a magnetic field along the diagonal perpendicular to the coil axes is significantly hampered. Indeed, as the magnetic field produced by a dipole source along its main axis is co-linear to this axis, this arrangement is highly unfavorable to generate a field perpendicular to these axes near the center of the region under consideration. The MFW is symmetric to the angle bisector for the first three angle values. These are essentially explained by the symmetry of the coils arrangement along the diagonal of the square region being analysed, and the symmetry of the desired set of tasks. The sets $\mathcal{I}$, $\mathcal{D}$ and $\mathcal{A}$ at the position P:$\begin{pmatrix} 0.025 & 0.025 \end{pmatrix}$ are illustrated in Fig. 2.

In Fig. 4b, the MFW is illustrated for four different distances between two parallel coils. The MFW gradually splits into two distinct regions after the third case. There seems to be an optimal arrangement around the second case where the MFW is the largest. Due to the symmetrical arrangement of the coils and the desired set of tasks, the MFW is symmetric to the horizontal line equidistant to the two coils axes.

In this simple case study, the use of the local and global evaluation metrics are illustrated in the arrangements depicted in Fig. 4a. The condition number and the $\mathcal{D}$-$\mathcal{A}$ distance within the MFW for the arrangement with $\theta = 90°$ are depicted in Fig. 4c. We can observe that the condition number is higher near the sources and along their main axis, because the field is relatively high along the source direction. With this in mind, it is understandable that the system is not as well conditioned at these positions, because this component is much easier to generate than those near the source. The $\mathcal{D}$-$\mathcal{A}$ distance is zero at the border of the workspace. This is because the limits of the workspace are composed of the positions where the inclusion (3) no longer holds, meaning that at least one of the tasks in $\mathcal{D}$ is not in $\mathcal{A}$, so that the distance to one of the hyperplane of $\mathcal{A}$ becomes negative.

Finally, the CGI_a for the configurations $\theta = \{45, 90, 135, 180\}°$ are, respectively, $\{0.30, 0.35, 0.44, 0.50\}$. This result is not necessarily intuitive; we would expect that the arrangements with the lower angles intrinsically provide a better dexterity overall, so that the CGI would decrease rather than increase with the angle. However, it is important to remember that the index is evaluated among the positions that are within the MFW, and that this is smaller for the higher angles due to the arrangement of the coils. In practice, in order to use the CGI to perform a fair comparison between two systems, the set of evaluated poses should be the same.

2) Four-coil systems: We investigate two arrangements of coils, with two pairs of co-linear and parallel coils, respectively. The co-linear arrangement is for example considered in [38] to manipulate magnetic suture needles, and has been shown as a possible arrangement to generate magnetic fields in a plane in [32]. The results for an eMNS composed of four coils in a planar arrangement is represented in Fig. 5.

We can observe that when the coils are co-linear (Fig. 5a), each quadrant within the square region (e.g. region denoted Q on the figure) has a similar shape as the two-coil system with an orthogonal arrangement ($\theta = 90°$ in Fig. 4a) up to a 90° rotation. This can be explained by the fact that the behavior
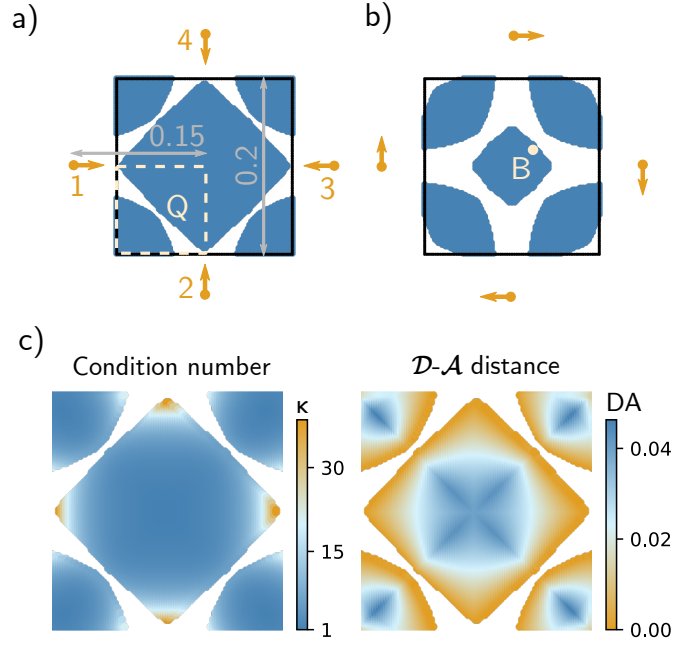

Fig. 5. MFW of an eMNS composed of four coils in a planar arrangement (for the sake of simplicity, these examples do not consider any physical units for the magnetic field magnitudes, the currents, and the distances). The positions within the MFW are represented in blue, and the dipole magnetic source of the coils are represented by the orange arrows. The tested area are the black squares with sides of 0.2 that is discretized with a 100×100 grid. The admissible currents are $\mathbf{\bar{i}} = -\mathbf{\underline{i}} = \begin{bmatrix} 1.0 & 1.0 & 1.0 & 1.0 \end{bmatrix}^T$ and the maximum field is $\bar{b} = -\underline{b} = 0.02$. a) An eMNS composed of two pairs of co-linear coils. b) An eMNS composed of two pairs of parallel coils. c) Condition number and $\mathcal{D}$-$\mathcal{A}$ distance for the arrangement with co-linear coils.

in each quadrant is mainly governed by the closest pair of orthogonal coils, and is barely affected by the more distant opposite pairs. For instance, the behavior in region Q is mainly governed by coils 1 and 2, and is barely affected by coils 3 and 4. Note the 4-fold symmetry in both cases. The shape of $\mathcal{A}$ at position labeled B in Fig. 5b is depicted in Fig. 3.

3) Interval analysis: As introduced in IV-C, interval analysis is a good alternative to discretization as a method to estimate the workspace of an eMNS. Interval analysis consists of testing the feasibility of full boxes in space rather than single positions as in the discretized method. For this we use the Rohn theorem, which allows us to make conclusions on the feasibility of an infinite number of linear systems of equations by testing the feasibility of only a finite number of equations [31]. We will now provide an application of this method and compare it to the results obtained via discretization. The interval analysis algorithm used here is adapted from the method introduced in [31] for cable-driven parallel robots. We consider the case of the two-coil planar system depicted in Fig. 4a for $\theta = 90°$ to illustrate this method. As an in-depth description of this method is outwith the scope of the paper, we will only explain the basic principles of interval analysis for this application. We encourage the interested reader to refer to the related reference and to our companion code (see appendix A) for more information on the details and implementation of this method.

We first perform the interval evaluation of the actuation matrix for a given region (also called *box*). The *interval matrix* obtained captures the range in which each component of the matrix evolves within each box. The interval matrix is then used to evaluate the feasibility of the box. For a task of dimension d, one must perform 2^d feasibility tests. Unlike the discretized case, feasibility tests in the context of interval analysis can lead to an inconclusive result, meaning that the box cannot be classified as either completely in or completely out of the workspace. In this case, the box is classified as *undetermined* until it is further bisected. Additionally, due to a so-called *wrapping effect*, the interval evaluation can also lead to an overestimation of the interval matrix which favors inconclusive results as well, even though the box could theoretically be properly classified with a more precise interval evaluation.
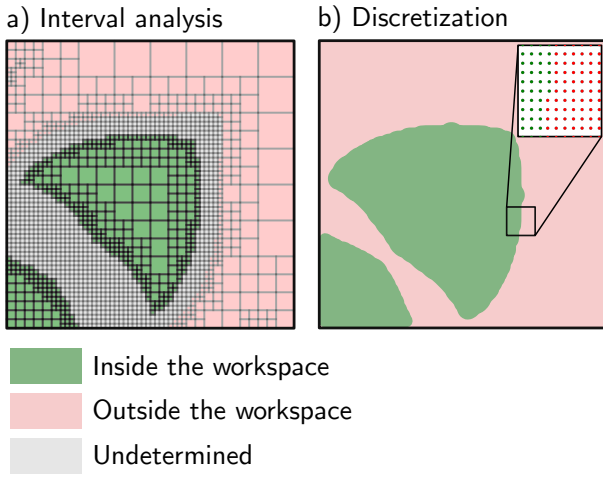

Fig. 6. Comparison between the use of interval analysis (a), and discretization (b) in the example of the workspace of a two-coil planar system depicted in Fig. 4a for $\theta = 90°$ (discretization grid of 100×100).

The tested boxes are bisected iteratively until their feasibility evaluation leads to a conclusive result, or their size are smaller than a minimum box size. Should the box not be classified by then, it will be considered as undetermined by the end of the procedure.

The results are depicted in Fig. 6. The discrete case considered a 100×100 grid. In contrast, the interval analysis method classified a total of 1735 boxes (448 inside, 315 outside, 972 undetermined) after 578 bisections, with a minimum box size set to 5.0×10^{-3}, and starting with an initial box consisting of the whole tested area (outer black square). As can be expected when using interval analysis, the workspace boundary is surrounded by undetermined boxes. This is due to the fact that the interval evaluation of the actuation matrix around this region does not allow for a conclusive classification of the box.

The performance of the method is strongly dependent on how well the interval matrix can be evaluated. This in turn determines how intensively the bisection must be performed around the workspace boundaries, to obtain box sizes that lead to a decisive result from the feasibility test. In our opinion, this constitutes the main disadvantage of this method.

This method allows the presence of holes in the workspace to be determined in the discrete case. We can confirm that both the inside and outside regions classified via interval analysis are indeed free of any holes when compared to the discrete case.

B. 3d systems

1) Three-coil system on a triangle base: We first illustrate the use of our method on an eMNS composed of three parallel coils on a triangular base. This configuration provides an open accessible volume while providing 3d field manipulation capability, as we later demonstrate with our experimental three-coil Navion eMNS in section VII. This also provides a natural extension in three dimensions of the 2d system illustrated in Fig. 4b, and gives a first comprehensive example of a 3d system with a simple arrangement yet with an interesting and non-trivial behavior.

In this example, we determine that admissible currents are between -3.0 and 3.0 and the desired magnetic task $\mathcal{D} = \{\mathbf{b} \in \mathbb{R}^3 \mid ||\mathbf{b}||_2 \leq \bar{b}\}$ with $\bar{b} = 0.02$. The results are depicted in Fig. 7.

We notice a similar separation of the workspace as the previous planar arrangement, with two parallel coils depicted in Fig. 4b. The MFW has a 3-fold symmetry due to the arrangement of the coils on a triangular base and the desired set of tasks.

2) Eight-coil system: We illustrate the MFW for three different magnetic tasks for an eMNS composed of eight coils, namely a task in a magnetic field, in a magnetic field gradient, and in a combination of both. This coil configuration is considered for several small- and medium-scale systems, such as the MiniMag or the OctoMag eMNS [15], [39] and is known to provide good 5-DOF navigation capabilities, as already demonstrated for various applications. We determine the admissible currents are between -1.0 and 1.0 in each coil and we considered three cases of desired set of tasks:

- $\mathcal{D} = \{\mathbf{b} \in \mathbb{R}^3 \mid ||\mathbf{b}||_2 \leq 0.09\}$
- $\mathcal{D} = \{\mathbf{g} \in \mathbb{R}^5 \mid ||\mathbf{g}||_2 \leq 0.5\}$
- $\mathcal{D} = \{(\mathbf{b}, \mathbf{g}) \in \mathbb{R}^8 \mid ||\mathbf{b}||_2 \leq 0.01 \ , \ ||\mathbf{g}||_2 \leq 0.05\}$

The results are depicted in Fig. 8 where the coils are represented by the orange cylinders.

Note that the MFW has a 4-fold symmetry due to the arrangement of the coils and the desired set of tasks.

C. Applications to the CardioMag eMNS

The CardioMag eMNS is composed of eight water-cooled electromagnets that can generate up to $35\,\mathrm{A}$, for a total power of $30\,\mathrm{kW}$. The system weights $7500\,\mathrm{kg}$. In the following, we calibrated the CardioMag (see Fig. 1a) using the approach proposed in [13], which uses a magnetic multipole expansion. The calibration process consists of placing a set of dipole sources that represent the contribution of each coil to the magnetic field. The model considered eight dipole sources per coil in order to account for cross-coupling between them.
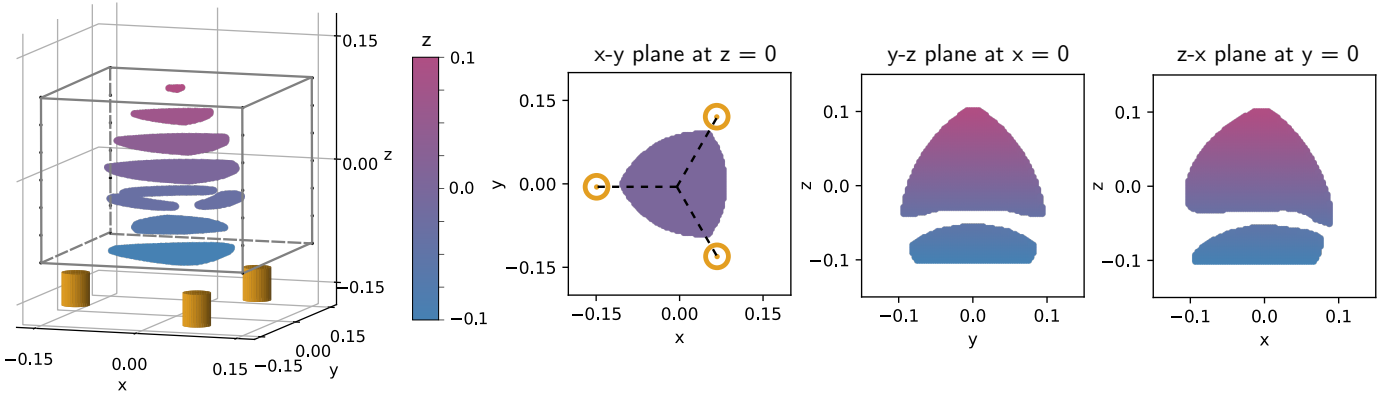
Fig. 7. MFW of an eMNS composed of three coils, represented by the orange cylinders, arranged on a triangular base. The feasibility is tested within seven horizontal slices, and two vertical slices of the cubic volume represented by the gray wire-frame on the 3d view on the left, each slice being discretized with a 100×100 grid. The color-scale represents the altitude z of the positions.
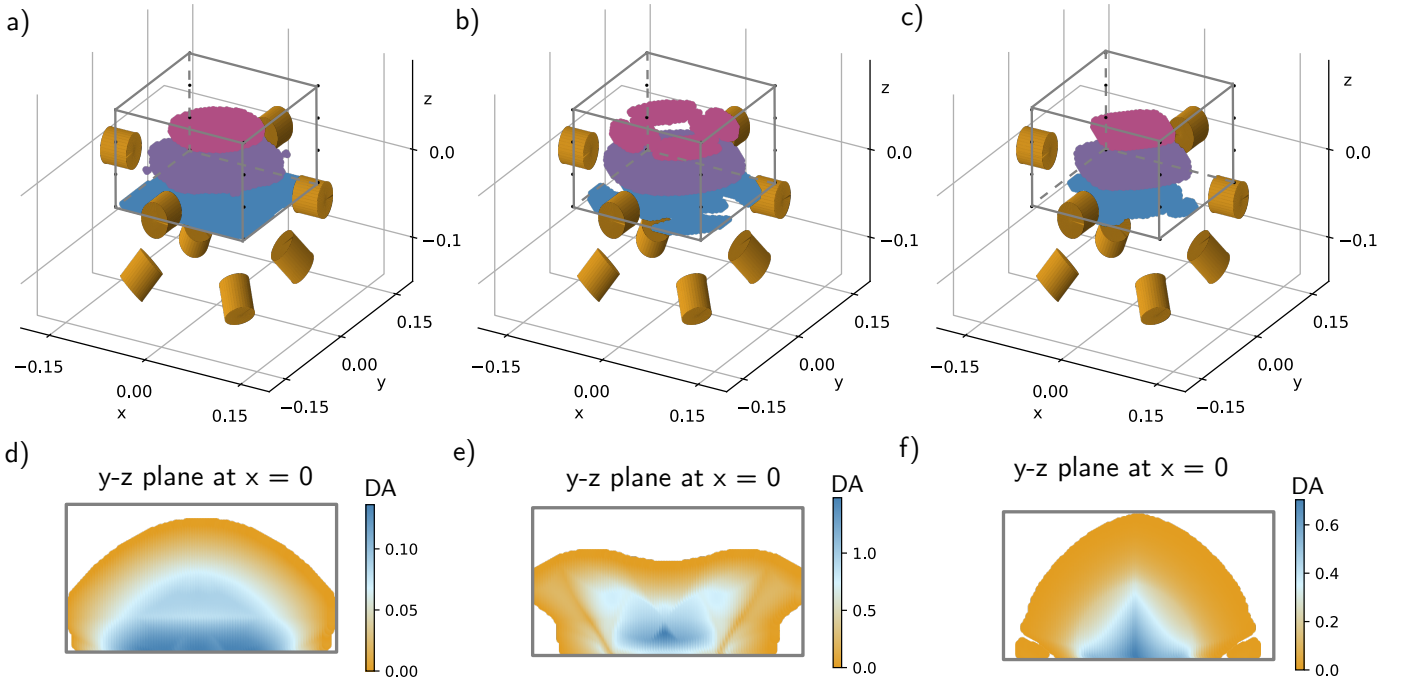

Fig. 8. MFW of an eMNS composed of eight coils. The feasibility is tested within three horizontal slices, and one vertical slice of the cubic volume represented by the gray wire-frame on the 3d view on the left, each slice being discretized with a 100×100 grid. The color-scale represents the altitude z of the positions (see Fig. 7). a) MFW for a magnetic task $\mathcal{D} = \{\mathbf{b} \in \mathbb{R}^3 \mid ||\mathbf{b}||_2 \leq 0.09\}$, b) $\mathcal{D} = \{\mathbf{g} \in \mathbb{R}^5 \mid ||\mathbf{g}||_2 \leq 0.5\}$, and c) $\mathcal{D} = \{(\mathbf{b}, \mathbf{g}) \in \mathbb{R}^8 \mid ||\mathbf{b}||_2 \leq 0.01 , ||\mathbf{g}||_2 \leq 0.05\}$, d)-f) $\mathcal{D}$-$\mathcal{A}$ distance within the MFWs in the $y - z$ plane at $x = 0$ for a)-c) respectively.

1) MFW and available magnetic field: We first illustrate the MFW obtained for a magnetic task $\boldsymbol{\tau} = \mathbf{b}$, and a desired task set $\mathcal{D} = \{\mathbf{b} \in \mathbb{R}^3 \mid ||\mathbf{b}||_2 \leq \bar{b}\}$ with $\bar{b} = 80\,\mathrm{mT}$. We show in Fig. 1b that a cube of side 0.1 m above the patient bed is entirely included within the MFW, meaning that a magnetic field of $80\,\mathrm{mT}$ in magnitude can be generated in any direction within this volume. The shape of the available magnetic field $\mathcal{A}$ at the center C of this cube is depicted in Fig. 1c. As a consequence of the hyperplane shifting method, the resulting shape of $\mathcal{A}$ is a polyhedron composed of eight pairs of parallel faces corresponding to the sixteen hyperplanes generated by each coil (one for the maximum and one for the minimum current). We can also see that the condition number κ increases significantly in the coils closer to the patient bed, thus indicating that the system is less isotropic within this region.

2) Case-study for cardiac catheter steering: In order to illustrate a practical use for our method, we consider the realistic task of steering a single-magnet magnetic catheter using the CardioMag eMNS. The navigation of a magnetic catheter consists of applying a magnetic torque to the magnet located at its tip in order to deform the flexible body of the catheter. In this case-study, we also want to ensure that this task can be performed without applying any additional
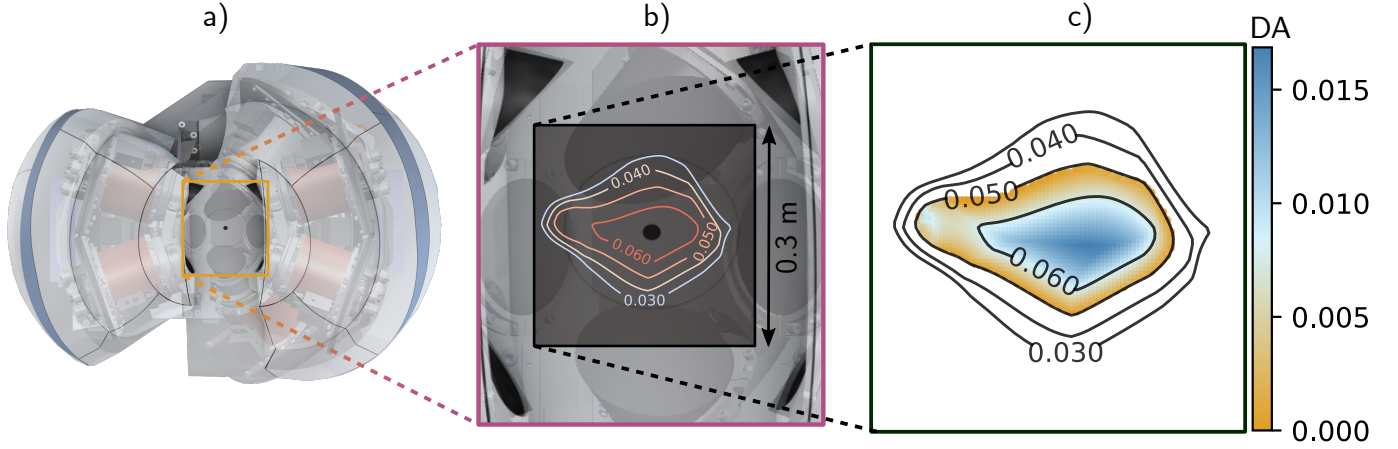
Fig. 9. Workspace analysis of the CardioMag eMNS for magnetic catheter navigation. a) Top view of the CardioMag eMNS. b) Isolines of the maximum achievable magnetic field magnitude in T within a $0.3\,\mathrm{m}$ side square at the level of the patient bed. c) Conservative estimate of the WFW (colored area), where a one-magnet cardiac catheter can be deflected up to $120°$ without a magnetic gradient (the maximum achievable magnetic field magnitude is overlaid on the same figure). The $\mathcal{D}$-$\mathcal{A}$ distance is represented by the colorscale.

magnetic forces on the magnet.

We consider the following constant curvature model that relates the magnetic torque magnitude t acting on a magnet of magnetic dipole magnitude m to the deflection θ of the catheter tip

$$t = \frac{\theta}{l} EI \qquad (30)$$

where E is the Young modulus of the catheter constitutive material, l its length, and I the second moment of area of the catheter's circular cross-section of diameter d. We consider the task of deflecting the catheter with a maximum tip angle $\bar{\theta} = 120°$ for any orientation of its proximal axis. The feasibility of this task is ensured if the desired task $\mathcal{D} = \{(\mathbf{b}, \mathbf{g}) \in \mathbb{R}^8 \mid ||\mathbf{b}||_2 \leq \bar{t}/m \ , \ \mathbf{g} \in \{\mathbf{0}_5\}\}$ is feasible, where $\bar{t}$ is the maximum torque to be generated on the catheter in order to achieve the tip deflection $\bar{\theta}$ according to (30). We consider the values $l = 40\,\mathrm{mm}$, $d = 2.3\,\mathrm{mm}$, $d = 22\,\mathrm{mN\,m\,T^{-1}}$, and $E = 15\,\mathrm{MPa}$ that correspond to a realistic one-magnet cardiac catheter.

The results for the WFW under these conditions are depicted in Fig. 9. Additionally, we represent the isolines of the maximum achievable magnetic field magnitude in every direction in the absence of gradient. This was computed using our feasibility method within a dichotomy algorithm to determine the maximum value of $\bar{b}$ for $\mathcal{D}$ to be feasible. We investigate the feasibility in a single plane on the patient bed within a square of side $0.3\,\mathrm{m}$, as depicted in Fig. 9b. The WFW is represented in Fig. 9c by the colored area. The border of the obtained WFW is close to the isoline of $50\,\mathrm{mT}$. Its shape does not exhibit a perfect symmetry. This is because the calibration is a result of an experimental process that does not constrain any symmetry in the placement of the dipole sources modeling the coils.

VII. EXPERIMENTAL VALIDATION

We provide an experimental validation of some of the previously introduced concepts on the Navion eMNS that is illustrated in Fig. 10a. Navion is a 450-kg eMNS composed of three liquid-cooled electromagnets arranged on a triangular base. The maximum power of the system is $32\,\mathrm{kW}$, with a maximum current of $35\,\mathrm{A}$ in each coil. The system has been primarily developed for magnetic remote endovascular navigation using soft magnetic tools. It provides suitable accessibility to the patient and for the integration of fluoroscopic imaging technologies. The system is calibrated using the approach proposed in [13].

We experimentally verify the maximum value of $\bar{b}$ within a calibrated region of the Navion eMNS, for a task $\boldsymbol{\tau} = \mathbf{b}$, and a desired task set $\mathcal{D} = \{\mathbf{b} \in \mathbb{R}^3 \mid ||\mathbf{b}||_2 \leq \bar{b}\}$. The maximum value of $\bar{b}$ at a given position, denoted b_{max} in the following, corresponds to the largest magnitude magnetic field that can be generated in any direction in space at this position. We determine that each coil can produce a current of up to $35\,\mathrm{A}$ in intensity, so that the set of admissible currents $\mathcal{I}$ can be represented as a cube of $70\,\mathrm{A}$ side depicted in Fig. 10c.

A. Approach

We consider the evaluation of b_{max} and $\mathcal{A}$ obtained with our methodology act as a ground truth. These are based on a magnetic model of the eMNS that can be evaluated at any position in a calibrated space. Our objective in this section is to estimate these experimentally. In the following, we denote $\tilde{b}_{max}$ and $\tilde{\mathcal{A}}$ the experimental estimates of b_{max} and $\mathcal{A}$ respectively.

The value b_{max} can be seen as the largest norm of magnetic field that can fit in $\mathcal{A}$ for any orientation of the field, or in other words the radius of the largest sphere that can be fully included in $\mathcal{A}$. Thus b_{max} can be determined as the smallest distance from the boundary of $\mathcal{A}$ to the origin of the magnetic frame (b_x, b_y, b_z). Recalling that our method generates $\mathcal{A}$ of
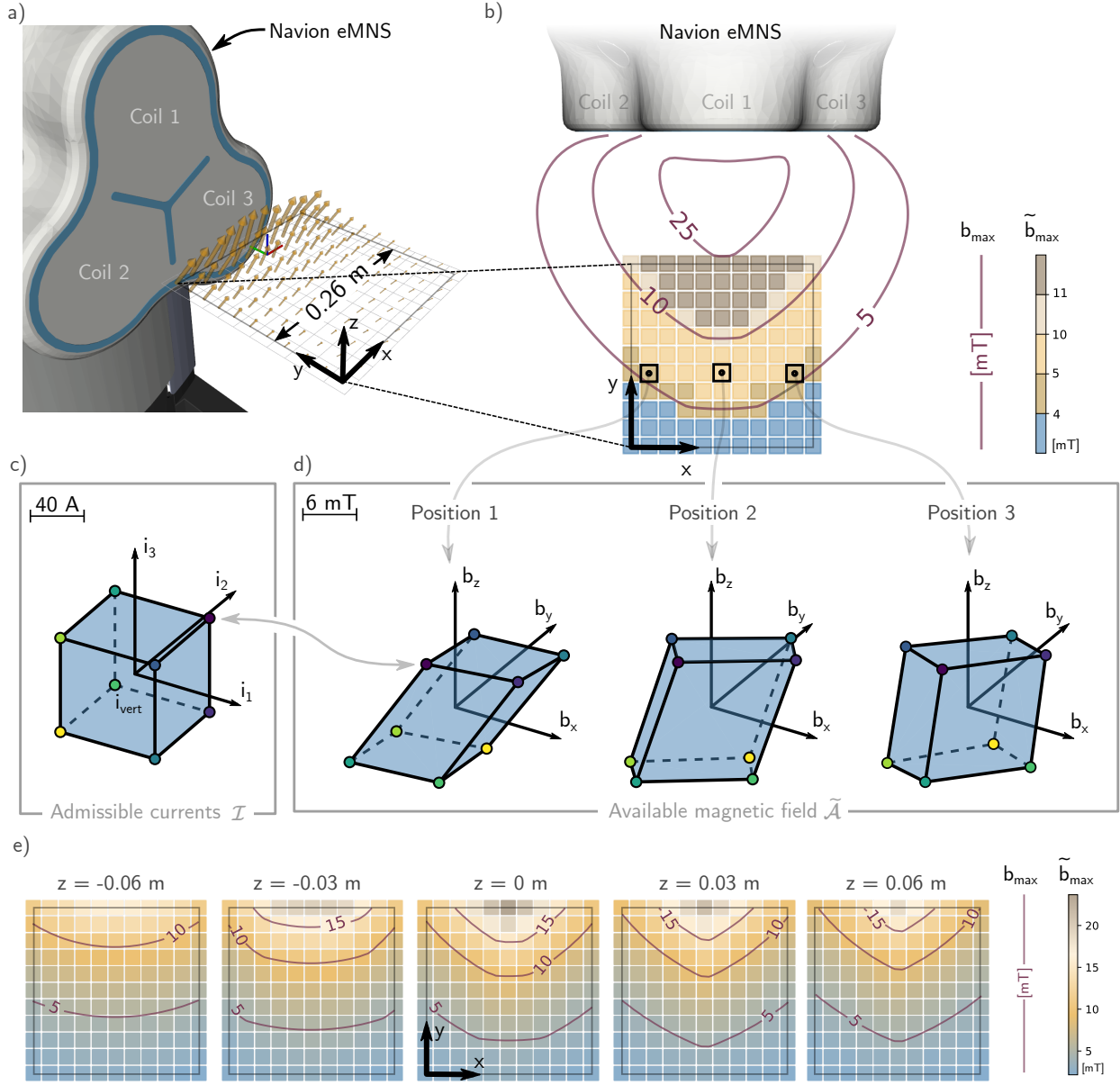
Fig. 10. Experimental validation on the Navion eMNS. a) Measured magnetic field with a 11×11 magnetometers' array for the current vector $\mathbf{i_{vert}} = \begin{bmatrix} 35 & 35 & -35 \end{bmatrix}^T$ A at the height $z = 0$. b) Experimental validation of the maximum field magnitude $\tilde{b}_{max}$ obtained at 121 positions. The isolines represent b_{max} in mT using the magnetic model of the Navion eMNS, and the colored scatter plot represents $\tilde{b}_{max}$ at the 121 sensors' positions. c) Admissible currents. d) Estimated available magnetic fields $\tilde{\mathcal{A}}$ at three different positions represented in b). e) Evaluation of $\tilde{b}_{max}$ at 121 positions and at five different heights (colored scatter plot). The isolines represent b_{max} in mT.

the form of convex polytopes (see for example Fig. 2), this distance corresponds to the distance of the closest face of $\mathcal{A}$ to the origin of the magnetic frame (b_x, b_y, b_z).

To evaluate $\tilde{b}_{max}$, it is thus necessary to estimate $\tilde{\mathcal{A}}$ first. To do so, we assume that $\tilde{\mathcal{A}}$ is a convex polytope as well, so that it can be obtained as the convex hull of its vertices, which map to the vertices of the admissible current set through the task actuation matrix. With this approach, the determination of $\tilde{\mathcal{A}}$ necessitates to generate the currents corresponding to the 8 vertices of $\mathcal{I}$, and to measure the corresponding magnetic fields at the positions in space where we want to compare $\tilde{b}_{max}$ to b_{max} (see colored vertices in Fig. 10c and d).

B. Setup

The magnetic field generated by the eMNS is measured by an 11×11 magnetometer array, where the 121 sensors (ALS31300, Allegro MicroSystems Inc.) are connected on an I^2C bus and arranged along a regular grid of 0.26×0.26 m in size. The array measures the 3d magnetic field at each grid position with an acquisition rate of 2.5 Hz. The coil currents are controlled via a computer running a Linux O.S. (Ubuntu 20.04), and using a Robotic Operating System interface (ROS Noetic) that communicates with the embedded computer of the eMNS via a TCP/IP protocol. The data are collected via ROS and include the target and measured currents in the coils, and the magnetic field measured by the magnetometer array.

An example of measurement is depicted in Fig. 10a on a customized ROS Vizualisation interface (RViz). The orange arrows represent the 3d magnetic fields measured by the magnetometers of the array for the current vector $\mathbf{i_{vert}}$ (see Fig. 10c).

C. Protocol

For each position, the determination of $\tilde{b}_{max}$ consists of the following protocol:

1) Generate the current targets corresponding to the vertices of $\mathcal{I}$ (colored corner-points in Fig. 10c).
2) Measure the 3d magnetic field corresponding to the vertices of $\tilde{\mathcal{A}}$ (colored corner-points in Fig. 10d).
3) Determine $\tilde{\mathcal{A}}$ as the convex hull of the measured vertices (blue envelopes in Fig. 10d).
4) Determine $\tilde{b}_{max}$ as the distance from the closest polygon of the convex hull to the origin of the magnetic frame (b_x, b_y, b_z).

Each current target was maintained for $5\,\mathrm{s}$ to ensure that steady-state was reached. The data were post-processed using Python scripting. An example of the measurements collected with the magnetometer array is depicted in Fig. 10a. In this example, the magnetic field is produced by the current vector $\mathbf{i_{vert}} = \begin{bmatrix} 35 & 35 & -35 \end{bmatrix}^T \mathrm{A}$ (see corresponding vertex in Fig. 10c).

D. Results

The scatter plot in Figure 10b shows the values of $\tilde{b}_{max}$ at each of the sensors' grid positions (the measures are at the center of the square marker). These results are in line with the values estimated via the magnetic model depicted by the isolines on the same figure. The available magnetic fields at three different positions within this grid are also illustrated in Fig. 10d. One can note that the system exhibits a symmetry which comes from the axial symmetry of the coil arrangement. This also explains why positions 1 and 3 exhibit a similar value for $\tilde{b}_{max}$, with their respective shape of $\tilde{\mathcal{A}}$ being mirrored along the plane of symmetry of the eMNS [7]. The measurements are repeated at 5 different heights (z-direction), and the results are depicted in Fig. 10e.

The values of $\tilde{b}_{max}$ at these 605 positions (11×11 grid points in 5 different planes) match the prediction of the magnetic model with a mean absolute error of $0.6\,\mathrm{mT}$. The absolute estimation error $|\tilde{b}_{max} - b_{max}|$ at four different heights at the magnetometers' positions is depicted in Fig. 11. This gives a comparison between the values obtained in simulation with the magnetic model, and their experimental estimation at the positions of the magnetometers. The error ranges from 1.0×10^{-3} to $1.3\,\mathrm{mT}$ and appears to be higher on average when z increases.

---

[7]The shape of the available set of tasks obtained here can be compared to the shape obtained for a similar magnetic task with the CardioMag eMNS as depicted in Fig. 1c, which exhibits a polyhedron with many more facets due to the higher number of coils of the eMNS.
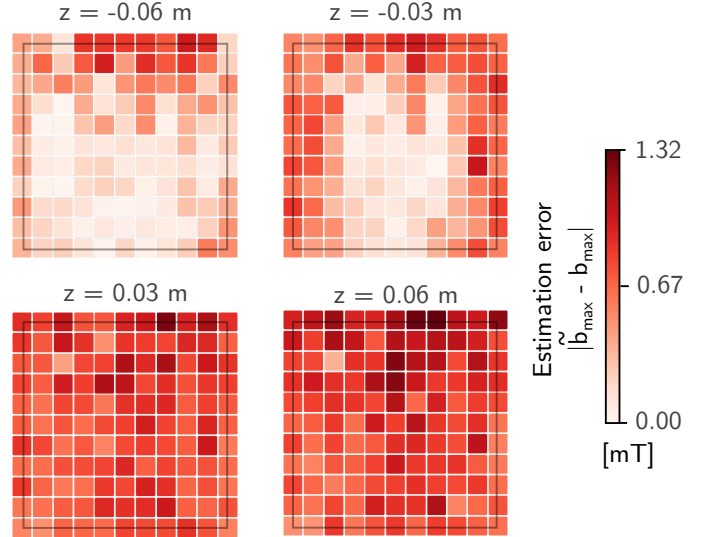

Fig. 11. Absolute estimation errors $|\tilde{b}_{max} - b_{max}|$ at the 121 positions of the magnetometers' array for four different heights of the array for the Navion eMNS. Measurements are compared with the linear magnetic model used for the calibration.

VIII. DISCUSSION

The algorithm introduced in section IV-A1 to evaluate the available set of tasks is suitable for an eMNS that can be modeled using linear magnetic models. This provides an efficient way to compute $\mathcal{A}$, which is useful regardless of the definition or even the concept of workspace. It can indeed be used to quickly determine at a given position what the eMNS is able to perform as a task, and even evaluate the feasibility of a position in real-time for control purposes. For tasks of dimensions lower or equal to three, this also constitutes as a useful method to provide a spatial representation of an available set in a convenient manner as the example depicted in Fig. 1c for the CardioMag eMNS. Our method to evaluate the feasibility, as well as the various definitions of the workspace introduced in this paper are generic, and can be applied to eMNSs with arbitrary number of coils [8].

In section VII, an experimental protocol inspired by this principle was derived in order to estimate the maximum magnetic field magnitude that can be generated in any direction in space. For an eMNS behaving in a linear manner, the available magnetic field can be determined as the convex hull of the magnetic fields generated at the vertices of the admissible current set. This was experimentally demonstrated on a three-coil eMNS, with an error lower than $1.3\,\mathrm{mT}$ compared to the estimation provided by a state-of-the-art linear model (less than 6% of the maximum field magnitude in the investigated region). The estimation error and its distribution over space depicted in Fig. 11 can be mainly explained by registration errors during the placement of the sensors array in front of the system. It can also be explained by the calibration errors of the magnetic model of the Navion eMNS, which are in the order of magnitude of the estimation errors reported in this

---

[8]under the restrictions discussed in [30] on the minimum number of coils needed to perform given tasks.

work. The results show that our method is able to estimate the maximum achievable field of the system in a consistent manner throughout space, and are in line with the theoretical values obtained by simulation (see Fig. 10b). Although the admissible error is highly dependent on the targeted application, we believe the present results are acceptable for the endovascular navigation of magnetic catheters, which is our main application target with the Navion eMNS. In this case, the required fields magnitude are of $25\,\text{mT}$ and above, and the maximum estimation error represents less than 5% of the field used for navigation.

Throughout this paper, we assume that the eMNS behaves in a linear manner. For systems with large ferromagnetic cores and high current densities, the magnetization response to coil current is, however, often significantly nonlinear, since the ferromagnetic material comprising the electromagnets exhibits magnetic saturation. In this case, nonlinear magnetic models, such as the ones introduced in [14], can be considered. The methodology introduced in IV-A1 is then only applicable for the analysis of these systems within their linear regime. In general, magnetic saturation and other effects leading to nonlinear behavior are limiting the performance of an eMNS as they reduce the maximum achievable field produced by a coil for a given current. For this reason, nonlinearities are expected to reduce the size of the workspaces defined in this work compared to systems operating with similar currents densities but free of these effects. Besides, the choice of the admissible set of currents in the coils in practice is constrained by the thermal losses in the coil's windings due to Joule heating. This can lead to high operating temperature of the coils, and limits the maximum achievable fields as well. For these reasons, for systems above a certain power, heat must usually be removed using additional fluid or air cooling systems.

As illustrated in section VI-A3, the use of interval analysis to iteratively estimate the workspace of an eMNS is an interesting alternative to the limitations of the discretized approach. The main advantage of interval analysis in this case, is to be able to verify whether a region in space is fully inside or outside of the workspace, thus discarding any issue related to holes in a given region that could be missed by discretization. The method is limited by the wrapping effect that usually prevents the accurate identification of the borders of the workspace where the boxes' classification remains undetermined. It is also quite cumbersome to apply to a non-2d case. We believe that the relevant use of the interval analysis lies in its combination with a discretization approach to test critical regions where the presence of holes must be avoided.

IX. CONCLUSION AND PERSPECTIVES

The definition of workspace for electromagnetic navigation systems, and its determination, are key aspects for further exploiting and comparing these robotic systems for medical applications. The determination of the feasibility of robotic tasks at a given set of positions is a central feature, and has been proposed here based on previous work on cable-driven parallel robots. Evaluation metrics introduced in this work provide both local and global indicators of their performance. These metrics allow for a fair and standardized comparison between different system designs, which can be used both for bench-marking and design optimization.

The code used to produce this work is available as a capsule on CodeOcean, and can be used and adapted to assess any calibrated system in a generic manner. The interested reader can also refer to appendix A for a more thorough explanation on which part of the code can be used to reproduce the results of this paper.

We believe that the definitions, methodology, and evaluation metrics presented in this paper constitute an important step toward a more unified framework for the design, comparison, and evaluation of eMNSs within the robotics research community.

APPENDIX A
DESCRIPTION OF THE SHARED CODE

The companion code to reproduce our results is available on CodeOcean (https://doi.org/10.24433/CO.2090933. v1). The CodeOcean capsule corresponds to the release v1.0.0 of the GitHub repository https://github.com/ethz-msrl/ Workspace_eMNS where our code is hosted. In the following, the locations of the files are provided within the folder /code/Workspace_eMNS/ of the repository:

- **Figure 1c**: the available magnetic field depicted in the figure is computed in 01_available_magnetic_field.ipynb.
- **Section IV-A1**: the hyperplane shifting method is implemented in the function `HyperPlaneShiftingMethod` in utilities.ipynb.
- **Section IV-A2**: the evaluation of the feasibility of the different types of set are implemented in the functions `VerifyFeasability*` in utilities.ipynb.
- **Section VI-A**: the examples with two and four coils are implemented in 02-00_2d_systems.ipynb, and the interval analysis of the two-coil system in 02-01_interval_ analysis.ipynb.
- **Section VI-B**: the examples with three and eight coils are implemented in 03_3d_systems.ipynb.
- **Section VI-C**: the application to the CardioMag eMNS is implemented in 04_cardiomag_application.ipynb.
- **Section VII**: the application to the Navion eMNS is implemented in 05_navion_application.ipynb and uses the experimental data stored in the folder /experimental_data for the comparison with the simulations.
- **Geometries of the eMNSs and magnetic models**: the magnetic models used for the different systems are available as *.yaml files in the folder /models. These files can be interpreted using the mag_manip Python package, and

the arrangement of the coils displayed with the functions `Coils2DPatch` and `PlotCoils3D` in utilities.ipynb.

APPENDIX B
ACRONYMS AND DEFINITIONS

A. Acronyms

RMN	Remote Magnetic Navigation
eMNS(s)	Electromagnetic Navigation System(s)
CDPR(s)	Cable-Driven Parallel Robot(s)
MFW	Magnetic-Feasible Workspace
WFW	Wrench-Feasible Workspace

B. Definitions

- **Magnetic task**: a task defined in terms of magnetic field and gradient to be generated by the eMNS.
- **Wrench task**: a task defined in terms of magnetic torques and forces to be applied on a magnetic object.
- **Set of admissible currents** ($\mathcal{I}$): (user-defined) set of currents restricting the value of the coil's currents.
- **Desired set of tasks** ($\mathcal{D}$): (user-defined) set of tasks that an eMNS must be able to achieve.
- **Available set of tasks** ($\mathcal{A}$): set composed of the tasks that can be achieved by the eMNS for a given set of admissible currents.
- **Tasks feasibility**: a desired set of tasks $\mathcal{D}$ is feasible by an eMNS if it is included in its available set of tasks $\mathcal{A}$ for a given set of admissible currents $\mathcal{I}$.
- **Magnetic-Feasible Workspace**: set of positions where a desired set of magnetic tasks is feasible, given a set of admissible currents.
- **Wrench-Feasible Workspace**: set of positions in space where a desired set of wrench tasks is feasible, given a set of admissible currents.

APPENDIX C
MATRIX FORMS FOR THE MAGNETIC FORCES AND TORQUES MAPPING

We consider that the magnetic dipole $\mathbf{m}$ of magnitude m is oriented in the base reference frame with the inclination and azimuth angles α and β (see Fig. 12), so that its coordinates in this frame are $m \begin{bmatrix} s_\alpha c_\beta & s_\alpha s_\beta & c_\alpha \end{bmatrix}^T$.
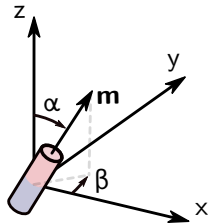

Fig. 12. Orientation of a dipole $\mathbf{m}$ in a base reference frame with inclination angle α and azimuth angle β.

The torques and forces that $\mathbf{m}$ experiences due to the magnetic field and its gradients are computed as

$$\mathbf{t} = \mathbf{T}(m, \alpha, \beta)\mathbf{b} \tag{31}$$

$$\mathbf{f} = \mathbf{F}(m, \alpha, \beta)\mathbf{g} \tag{32}$$

with the following matrices

$$\mathbf{T} = m \begin{bmatrix} 0 & -c_\alpha & s_\alpha s_\beta \\ c_\alpha & 0 & -s_\alpha c_\beta \\ -s_\alpha s_\beta & s_\alpha c_\beta & 0 \end{bmatrix} \tag{33}$$

$$\mathbf{F} = m \begin{bmatrix} s_\alpha c_\beta & s_\alpha s_\beta & c_\alpha & 0 & 0 \\ 0 & s_\alpha c_\beta & 0 & s_\alpha s_\beta & c_\alpha \\ -c_\alpha & 0 & s_\alpha c_\beta & -c_\alpha & s_\alpha s_\beta \end{bmatrix} \tag{34}$$

where s_a and c_a abbreviate the sine and cosine of an angle a, and α and β are the inclination and azimuth angle of the vector $\mathbf{m}$ in the reference frame, and m is the magnitude of the dipole moment.

REFERENCES

[1] J. J. Abbott, E. Diller, and A. J. Petruska, "Magnetic Methods in Robotics," *Robotics, and Autonomous Systems*, vol. 19, no. 4, 2019.

[2] J. Li, B. Ávila, W. Gao, L. Zhang, and J. Wang, "Micro/nanorobots for Biomedicine: Delivery, surgery, sensing, and detoxification," *Science Robotics*, vol. 2, no. 4, 3 2017.

[3] N. Ebrahimi, C. Bi, D. J. Cappelleri, G. Ciuti, A. T. Conn, D. Faivre, N. Habibi, A. Hošovský, V. Iacovacci, I. S. M. Khalil, V. Magdanz, S. Misra, C. Pawashe, R. Rashidifar, P. E. D. Soto-Rodriguez, Z. Fekete, and A. Jafari, "Magnetic Actuation Methods in Bio/Soft Robotics," *Advanced Functional Materials*, vol. 31, no. 11, p. 2005137, 3 2021.

[4] Y. Kim, G. A. Parada, S. Liu, and X. Zhao, "Ferromagnetic soft continuum robots," *Science Robotics*, vol. 4, p. 7329, 2019.

[5] S. L. Charreyron, Q. Boehler, A. Danun, A. Mesot, M. Becker, and B. J. Nelson, "A Magnetically Navigated Microcannula for Subretinal Injections," *IEEE Transactions on Biomedical Engineering*, vol. 68, no. 1, 2020.

[6] C. M. Hendricks, M. S. Cavilla, D. E. Usevitch, T. L. Bruns, K. E. Riojas, L. Leon, R. J. Webster III, F. M. Warren, and J. J. Abbott, "Magnetic Steering of Robotically Inserted Lateral-wall Cochlear-implant Electrode Arrays Reduces Forces on the Basilar Membrane In Vitro," *Otology \& Neurotology*, vol. 42, no. 7, pp. 1022–1030, 2021.

[7] A. Hong, A. J. Petruska, A. Zemmar, and B. J. Nelson, "Magnetic Control of a Flexible Needle in Neurosurgery," *IEEE Transactions on Biomedical Engineering*, vol. 68, no. 2, pp. 616–627, 2 2021.

[8] J. Lussi, M. Mattmann, S. Sevim, F. Grigis, C. De Marco, C. Chautems, S. Pané Vidal, J. Puigmartí-Luis, Q. Boehler, and B. Nelson, "A Submillimeter Continuous Variable Stiffness Catheter for Compliance Control," *Advanced Science*, vol. 8, no. 18, 2021.

[9] C. Zhou, Y. Yang, J. Wang, Q. Wu, Z. Gu, Y. Zhou, X. Liu, Y. Yang, H. Tang, Q. Ling, L. Wang, and J. Zang, "Ferromagnetic soft catheter robots for minimally invasive bioprinting," *Nature Communications*, vol. 12, no. 1, 2021.

[10] J. Rahmer, C. Stehning, and B. Gleich, "Spatially selective remote magnetic actuation of identical helical micromachines," *Science Robotics*, vol. 2, no. 3, 2 2017.

[11] F. Carpi and C. Pappone, "Stereotaxis Niobe® magnetic navigation system for endocardial catheter ablation and gastrointestinal capsule endoscopy," *Expert Review of Medical Devices*, vol. 6, no. 5, pp. 487–498, 9 2009.

[12] G. Bassil, S. M. Markowitz, C. F. Liu, G. Thomas, J. E. Ip, B. B. Lerman, and J. W. Cheung, "Robotics for catheter ablation of cardiac arrhythmias: Current technologies and practical approaches," *Journal of Cardiovascular Electrophysiology*, vol. 31, no. 3, pp. 739–752, 3 2020.

[13] A. J. Petruska, J. Edelmann, and B. J. Nelson, "Model-Based Calibration for Magnetic Manipulation," *IEEE Transactions on Magnetics*, vol. 53, no. 7, 2017.

[14] S. L. Charreyron, Q. Boehler, B. Kim, C. Weibel, C. Chautems, and B. J. Nelson, "Modeling Electromagnetic Navigation Systems," *IEEE Transactions on Robotics*, vol. 37, no. 1, pp. 1009–1021, 2021.

[15] M. P. Kummer, J. J. Abbott, B. E. Kratochvil, R. Borer, A. Sengul, and B. J. Nelson, "Octomag: An electromagnetic system for 5-DOF wireless micromanipulation," *IEEE Transactions on Robotics*, vol. 26, no. 6, pp. 1006–1017, 2010.

[16] J. Sikorski, I. Dawson, A. Denasi, E. E. G. Hekman, and S. Misra, "Introducing BigMag - A novel system for 3D magnetic actuation of flexible surgical manipulators," in *Proceedings - IEEE International Conference on Robotics and Automation*. Institute of Electrical and Electronics Engineers Inc., 2017, pp. 3594–3599.

[17] A. Pourkand and J. J. Abbott, "A Critical Analysis of Eight-Electromagnet Manipulation Systems: The Role of Electromagnet Configuration on Strength, Isotropy, and Access," *IEEE Robotics and Automation Letters*, vol. 3, no. 4, pp. 2957–2962, 10 2018.

[18] F. Niu, J. Li, W. Ma, J. Yang, and D. Sun, "Development of an Enhanced Electromagnetic Actuation System with Enlarged Workspace," *IEEE/ASME Transactions on Mechatronics*, vol. 22, no. 5, pp. 2265–2276, 10 2017.

[19] X. Du, L. Yang, J. Yu, K. F. Chan, P. W. Y. Chiu, and L. Zhang, "RoboMag: A Magnetic Actuation System Based on Mobile Electromagnetic Coils with Tunable Working Space," in *ICARM 2020 - 2020 5th IEEE International Conference on Advanced Robotics and Mechatronics*. Institute of Electrical and Electronics Engineers Inc., 12 2020, pp. 125–131.

[20] D. Dong, W. S. Lam, and D. Sun, "Electromagnetic Actuation of Microrobots in a Simulated Vascular Structure with a Position Estimator Based Motion Controller," *IEEE Robotics and Automation Letters*, vol. 5, no. 4, pp. 6255–6261, 10 2020.

[21] L. Zheng, Y. Jia, D. Dong, W. Lam, D. Li, H. Ji, and D. Sun, "3D Navigation Control of Untethered Magnetic Microrobot in Centimeter-Scale Workspace Based on Field-of-View Tracking Scheme," *IEEE Transactions on Robotics*, vol. 38, no. 3, pp. 1583–1598, 11 2021.

[22] A. Chah, T. Kroubi, and K. Belharet, "A new electromagnetic actuation system with a highly accessible workspace for microrobot manipulation," in *IEEE/ASME International Conference on Advanced Intelligent Mechatronics, AIM*, vol. 2020-July. Institute of Electrical and Electronics Engineers Inc., 7 2020, pp. 723–728.

[23] L. Manamanchaiyaporn, T. Xu, and X. Wu, "An optimal design of an electromagnetic actuation system towards a large homogeneous magnetic field and accessibleworkspace for magnetic manipulation," *Energies*, vol. 13, no. 4, p. 911, 2 2020.

[24] Z. Yang, L. Yang, and L. Zhang, "Autonomous Navigation of Magnetic Microrobots in a Large Workspace Using Mobile-Coil System," *IEEE/ASME Transactions on Mechatronics*, vol. 26, no. 6, pp. 3163–3174, 12 2021.

[25] B. Roth, "Performance Evaluation of Programmable Robots and Manipulators," *NBS Special Publication*, vol. 459, pp. 39–62, 1976.

[26] E. J. Haug, C.-M. Luh, F. A. Adkins, and J.-Y. Wang, "Numerical Algorithms for Mapping Boundaries of Manipulator Workspaces," *J Mech Design*, vol. 118, no. 2, pp. 228–234, 1996.

[27] I. Ebert-Uphoff and P. Voglewede, "On the connections between cable-driven robots, parallel manipulators and grasping," in *Robotics and Automation (ICRA), 2004 IEEE International Conference on*, vol. 5. IEEE, 2004, pp. 4521–4526.

[28] S. Bouchard, C. Gosselin, and B. Moore, "On the ability of a cable-driven robot to generate a prescribed set of wrenches," *ASME J Mech Robot*, vol. 2, no. 1, p. 11010, 12 2009.

[29] S. Afshar, M. B. Khamesee, and A. Khajepour, "Optimal configuration for electromagnets and coils in magnetic actuators," *IEEE Transactions on Magnetics*, vol. 49, no. 4, pp. 1372–1381, 2013.

[30] A. J. Petruska and B. J. Nelson, "Minimum Bounds on the Number of Electromagnets Required for Remote Magnetic Manipulation," *IEEE Transactions on Robotics*, vol. 31, no. 3, pp. 714–722, 2015.

[31] M. Gouttefarde, D. Daney, and J. P. Merlet, "Interval-analysis-based determination of the wrench-feasible workspace of parallel cable-driven robots," *IEEE Transactions on Robotics*, vol. 27, no. 1, pp. 1–13, 2011.

[32] S. Erni, S. Schürle, A. Fakhraee, B. E. Kratochvil, and B. J. Nelson, "Comparison, optimization, and limitations of magnetic manipulation systems," *J Micro-Bio Robot*, vol. 8, pp. 107–120, 2013.

[33] C. R. Thornley, L. N. Pham, and J. J. Abbott, "Reconsidering Six-Degree-of-Freedom Magnetic Actuation Across Scales," *IEEE Robotics and Automation Letters*, vol. 4, no. 3, pp. 2325–2332, 7 2019.

[34] R. Chen, D. Folio, and A. Ferreira, "Mathematical approach for the design configuration of magnetic system with multiple electromagnets," *Robotics and Autonomous Systems*, vol. 135, 1 2021.

[35] T. Yoshikawa, "Manipulability of Robotic Mechanisms," *The International Journal of Robotics Research*, vol. 4, pp. 3–9, 1985.

[36] J. P. Merlet, "Jacobian, Manipulability, Condition Number, and Accuracy of Parallel Robots," *Journal of Mechanical Design*, vol. 128, no. 1, p. 199, 2006.

[37] F. Guay, P. Cardou, A. L. Cruz-Ruiz, and S. Caro, "Measuring how well a structure supports varying external wrenches," in *Mechanisms and Machine Science*, vol. 17. Kluwer Academic Publishers, 1 2014, pp. 385–392.

[38] L. O. Mair, X. Liu, B. Dandamudi, K. Jain, S. Chowdhury, J. Weed, Y. Diaz-Mercado, I. N. Weinberg, and A. Krieger, "MagnetoSuture: Tetherless Manipulation of Suture Needles," *IEEE Transactions on Medical Robotics and Bionics*, vol. 2, no. 2, pp. 206–215, 5 2020.

[39] B. E. Kratochvil, M. P. Kummer, S. Erni, R. Borer, D. R. Frutiger, S. Schürle, and B. J. Nelson, "MiniMag: A hemispherical electromagnetic system for 5-DOF wireless micromanipulation," in *Springer Tracts in Advanced Robotics*, vol. 79. Springer Verlag, 2014, pp. 317–329.

Quentin Boehler Quentin Boehler received a master's degree in mechatronics from INSA Strasbourg, France in 2013, and a Ph.D. degree in robotics from the University of Strasbourg, France in 2016. He joined the Multi-Scale Robotics Lab at ETH Zurich in 2017 and is currently a senior scientist. His research interests include magnetic actuation for medical robotics, the development and analysis of electromagnetic navigation systems, and the design and control of soft magnetic robots.

Simone Gervasoni Simone Gervasoni received a M.Sc. in mechanical engineering in 2015 from ETH Zurich. He joined the Multi-Scale Robotics Lab at ETH Zurich in 2016 and completed his Ph.D. in 2022 under the supervision of Prof. Brad Nelson. During his Ph.D., he investigated new approaches to design electromagnetic navigation systems and their integration in a clinical workspace. Currently he is developing the newest generation of high power densities eMNS.

Samuel L. Charreyron Samuel Charreyron received the B.Eng. degree in electrical engineering from McGill University, Montreal, Quebec, Canada, in 2012, the M.Sc. in electrical engineering from ETH Zurich, Zurich, Switzerland, in 2014. He joined the Multi-Scale Robotics Lab, ETH Zurich, in 2013 as a Masters Student and completed the Ph.D. degree under the supervision of Prof. B. Nelson where he researched applications of magnetic navigation for minimally invasive surgery.

Christophe Chautems Christophe Chautems studied mechanical engineering at ETH Zurich. Between 2009 and 2011, he was involved in a research project at Nasa Ames and at ESA. He worked for the automotive industry before joining Aeon Scientific to develop an electro-magnetic navigation system to steer a catheter for cardiac arrhythmia ablations. He joined the MSRL in 2016 with the intention of shaping the future of magnetic navigation technology for applications in the medical field.

Bradley J. Nelson Brad Nelson (M'90, SM'06, F'11) received the B.S. degree in Mechanical Engineering from the University of Illinois at Urbana-Champaign in 1984, the M.S. degree in Mechanical Engineering from the University of Minnesota in 1987, and the Ph.D. degree in Robotics from the School of Computer Science, Carnegie-Mellon University, Pittsburgh, PA, in 1995. He has been the Professor of Robotics and Intelligent Systems at ETH Zürich since 2002, where his research focuses on micro and nanorobotics with applications in biology and medicine. He has received a number of awards for his work in robotics, nanotechnology, and biomedicine.